Characteristics of breaking irregular wave forces on a monopile

Ankit Aggarwal*[1], Hans Bihs[1], Dag Myrhaug[2], and Mayilvahanan Alagan Chella[3]

[1]Department of Civil and Environmental Engineering, Norwegian University of Science and Technology (NTNU), 7491 Trondheim, Norway
[2]Department of Marine Technology, Norwegian University of Science and Technology (NTNU), 7491 Trondheim, Norway
[3]Department of Civil and Environmental Engineering and Earth Sciences, University of Notre Dame, Indiana, USA

Abstract

The substructures of offshore wind turbines are subjected to extreme breaking irregular wave forces. The present study is focused on investigating breaking irregular wave forces on a monopile using a computational fluid dynamics (CFD) based numerical model. The breaking irregular wave forces on a monopile mounted on a slope are investigated with a numerical wave tank. The experimental and numerical irregular free surface elevations are compared in the frequency-domain for the different locations in the vicinity of the cylinder. A numerical analysis is performed for different wave steepness cases to understand the influence of wave steepness on the breaking irregular wave loads. The wave height transformation and energy level evolution during the wave shoaling and wave breaking processes is investigated. The higher-frequency components generated during the wave breaking process are observed to play a significant role in initiating the secondary force peaks. The free surface elevation skewness and spectral bandwidth during the wave transformation process are analysed and an investigation is performed to establish a correlation of these parameters with the breaking irregular wave forces. The role of the horizontal wave-induced water particle velocity at the free surface and free surface pressure in determining the breaking wave loads is highlighted. The higher-frequency components in the velocity and pressure spectrum are observed to be significant in influencing the secondary peaks in the breaking wave force spectrum.

Keywords: irregular breaking wave loads; skewness; spectrum; monopile; wave deformation

1 Introduction

Offshore wind technology has experienced a remarkable growth due to an increased focus towards the green and renewable energy research. The objective of offshore wind related research is to develop methods of design and construction which will help to keep offshore wind turbines safe, efficient, functional, economical and able to resist the severe environmental loads. Among the environmental loads, wave loads are very important for the design of the offshore wind turbines. They are exposed to irregular and severe sea states which are composed of both breaking and non-breaking waves. Usually, wave breaking occurs when waves propagate from deep water to shallow water. The wave height increases until the wave crest becomes vertical and overturns with a jet of water. Due to the overturning crest and the large amount of water impacting the cylinder, breaking waves exert large impact loads, which is crucial in design of offshore wind turbines (Det Norske Veritas (DNV), 2010). Ocean waves exhibit a random behaviour. Each individual wave component in the irregular wave train possesses a distinctive wave height and period, which influences the breaking pattern for each wave. Consequently, the breaking location, breaker height and breaking wave forces vary for each individual wave (Rattanapitikon and Shibayama, 1998). The energy transfers towards the higher frequencies, which occurs during the wave transformation, influences the characteristics of the wave spectrum which in turn affects the breaking irregular wave loads. Several experiments and field studies have been conducted to study the breaking regular wave forces in shallow water. Goda et al. (1966) concluded that the change in momentum of the water mass of a vertical wave front causes the impact force by performing experiments on a vertical cylinder. Tanimoto et al. (1986) conducted experiments for inclined piles under irregular waves and proposed a method to calculate the impact forces by using the simplified von Karman's and Wagner's theory. Apelt and Piorewicz (1987) carried out experiments for measuring the breaking regular wave forces by placing a cylinder in the surf zone. They expressed the forces as a function of deep water wave steepness and dimensionless cylinder diameter. Chan and Melville (1988) correlated the impact force history with the position of the breaking point measured with respect to the location of the structure front, and hence by the breaker shape. Oumeraci et al. (1993) conducted experiments to point out that the breaking criteria for regular waves on unobstructed flat sea bottoms cannot be applied for incident irregular waves on vertical structures. Chakrabarti et al. (1997) measured breaking wave forces on a single pile caisson in breaking waves for both regular and irregular waves. They investigated the changes in the wave energy spectra during the wave breaking process and the breaking irregular wave forces in the time-domain.

Numerical modelling with computational fluid dynamics (CFD) can be used to study the breaking waves and breaking wave forces. Many important hydrodynamic flow details can be modelled by using CFD with interface capturing and two-phase flow, which are difficult to measure in the experiments. Several researchers have numerically modelled breaking waves and associated forces in the past (Lin and Liu, 1998; Zhao et al., 2004; Hieu et al., 2004; Jacobsen et al., 2012; Mo et al., 2013; Choi et al., 2015). The modelling of breaking waves is quite challenging due to the higher-order and non-linear wave transformations during the wave breaking process. Most of the numerical studies are dedicated towards the modelling of regular breaking waves and wave forces. Kamath et al. (2016a) modelled breaking regular wave forces on a vertical cylinder. They validated their numerical model by comparing their results with experiments with a good accuracy. They further investigated the effect of

breaking location on the breaking wave forces. Christensen et al. (2005) and Bredmose and Jacobsen (2010) investigated the breaking wave forces under focused waves and regular waves on offshore wind turbine foundations, respectively, and reported reasonably good results. Alagan Chella et al. (2017); Bihs et al. (2016b) have numerically investigated breaking regular and solitary waves and wave forces on a single cylinder and tandem cylinders. They found good agreement with the experimental breaking wave force data. Although a few researchers have numerically modelled non-breaking irregular wave forces (Aggarwal et al., 2016a,b; Paulsen et al., 2013), there are no CFD studies performed to investigate the breaking irregular wave forces and the associated spectral characteristics to the best of the authors' knowledge. The breaking irregular waves are complicated in nature compared to the breaking regular waves due to the multiple frequencies, wider breaking area and multiple breaker heights.

The goal of the present work is to investigate breaking irregular wave forces and associated characteristics on a vertical cylinder mounted on a slope in the frequency-domain. The numerical simulations are performed with the open-source hydrodynamics model REEF3D (Bihs et al., 2016a). The numerical model has been validated for different applications including breaking regular wave forces (Kamath et al., 2016b; Alagan Chella et al., 2016; Kamath et al., 2017). The numerical model is first evaluated for the irregular wave surface elevation and then, breaking irregular wave forces on a vertical cylinder for two cases for three different grid sizes. Both cases are compared with the experiments performed by Chakrabarti et al. (1997). The numerical results agree well with the experimental measurements. Further, numerical simulations are performed for different cases (based on different wave steepnesses) to investigate the wave transformations during the wave breaking process. The wave spectra and the wave heights at the different wave gauge locations around the cylinder are investigated to understand the energy level evolution during wave breaking process. Further, the breaking irregular wave forces are analysed in the frequency-domain and the effect of the higher-frequency wave components on the wave forces is discussed. The role of the free surface elevation skewness and spectral bandwidth in influencing the irregular breaking wave forces is investigated. The influence of wave deformation and wave breaking location on determining the wave breaker type is studied by exploring the geometric wave profile properties and breaker indices. The horizontal wave-induced water particle velocity at the free surface is also an important factor in determining the free surface pressure and consequently, the breaking wave forces. Therefore, the spectral variations of the free surface velocity and free surface pressure are examined in the frequency-domain to understand the transformation of horizontal wave-induced water particle velocity and wave pressure during the breaking process. Further, the best distribution fit is also determined for the breaker indices, significant value of the irregular breaking wave force and peak free surface pressure to understand their statistics.

2 Numerical Model

2.1 Governing Equations

In the present work, the open-source hydrodynamics model REEF3D (Bihs et al., 2016a; Bihs and Kamath, 2017) is employed. The numerical model is based on the Reynolds-Averaged Navier-Stokes equations (RANS) defined for incompressible fluids. The governing equations

are the momentum conservation equation and the continuity equation:

$$\frac{\partial u_i}{\partial x_i} = 0 \tag{1}$$

$$\frac{\partial u_i}{\partial t} + u_j \frac{\partial u_i}{\partial x_j} = -\frac{1}{\rho}\frac{\partial P}{\partial x_i} + \frac{\partial}{\partial x_j}\left[(\nu + \nu_t)\left(\frac{\partial u_i}{\partial x_j} + \frac{\partial u_j}{\partial x_i}\right)\right] + g_i \tag{2}$$

where u is the velocity averaged over time t, ρ is the fluid density, P is the pressure, ν is the kinematic viscosity, ν_t is the eddy-viscosity and g is the acceleration due to gravity.

For the spatial discretization, the fifth-order finite difference Weighted Essentially Non-Oscillatory (WENO) scheme in multi-space dimensions is used (Jiang and Shu, 1996). The viscous terms are source term dependent and result in very low CFL numbers when discretised explicitly. In order to avoid this, the viscous terms are treated with an implicit method to take it out of the CFL criterion. The third-order TVD Runge Kutta scheme is used for time discretization (Shu and Oscher, 1988). An adaptive time stepping is applied in order to control the CFL number and computing the time step size (Griebel et al., 1998). The pressure in the Navier-Stokes equations is computed using the projection method (Chorin, 1968). The HYPRE integrated conjugate gradient solver in combination with the multigrid preconditioning is utilized to solve the Poisson pressure equation (Falgout and Yang, 2002). The present study uses the $k - \omega$ model (Wilcox, 1994) along with the RANS equation to solve for turbulence. The numerical model employs a Cartesian grid approach in order to apply the higher-order discretization schemes. A ghost cell immersed boundary method (GCIBM) is applied in order to implement the irregular and non-orthogonal solid boundaries (Berthelsen and Faltinsen, 2008). For capturing the free surface, the level set method approach (Osher and Sethian, 1988) is used. The level set function gives the closest distance to the interface and the two phases are distinguished by the change of the sign. The function can be written as:

$$\phi(\vec{x}, t) \begin{cases} > 0 & if \ \vec{x} \text{ is in phase 1} \\ = 0 & if \ \vec{x} \text{ is at the interface} \\ < 0 & if \ \vec{x} \text{ is in phase 2} \end{cases} \tag{3}$$

A higher-order discretization scheme for the convection of the level set equation as mentioned above, in combination with the staggered grids results in insignificant mass loss in the numerical wave tank. The mass conservation with the present numerical model has been shown in Alagan Chella et al. (2016). At the interface, the fluid properties such as the density and viscosity are smoothened across the interface over a distance of $2.1dx$ using a Heaviside function. The details of the density and viscosity interpolation are presented in Bihs et al. (2016a).

2.2   Irregular wave generation

In the present work, the relaxation method is used for the wave generation (Mayer et al., 1998), and they are dissipated with the active wave absorption method at the outlet boundary (Schaffer and Klopman, 2000). Wall boundary conditions are used on the sides of the NWT. The irregular waves are generated by superposition of linear regular waves components. The free surface η is defined as:

$$\eta = \sum_{i=1}^{N} A_i cos\theta_i \tag{4}$$

$$A_i = \sqrt{2S(\omega_i)\Delta\omega_i} \tag{5}$$

$$\theta_i = k_i x - \omega_i t + \epsilon_i \tag{6}$$

$$\omega_i^2 = gk_i\tanh k_i d \tag{7}$$

where N is the number of components, d is the water depth, A_i is the amplitude of the each wave component, $S(\omega_i)$ is the spectral density and θ_i is the phase of the each component, ϵ_i is a random number distributed between 0 and 2π, ω_i is the angular wave frequency, λ_i is the wavelength of a component and k_i is the wave number of a component given by:

$$k_i = \frac{2\pi}{\lambda_i} \tag{8}$$

Similarly, the horizontal velocity u and the vertical velocity w are computed as the superposition of the individual u_i and w_i components in the irregular wave train. In the present study, the Bretschneider spectrum is used for the generation of irregular waves. The Bretschneider spectrum is mainly defined for the developed sea states. The input values to the spectrum are the significant wave height H_s and the peak angular frequency ω_p:

$$S(\omega) = \frac{5}{16}H_s^2\frac{\omega_p^4}{\omega^5}exp[\frac{-5}{4}(\frac{\omega_p}{\omega})^4] \tag{9}$$

2.3 Wave force computation

The total wave force (F) in the numerical model is calculated by integrating the pressure and the normal component of viscous stress tensor τ over the surface Ω of the structure. This procedure is performed discretely by evaluating the pressure p and τ for the individual cell surfaces:

$$\mathbf{F} = \int_\Omega (-\mathbf{n}p + \mathbf{n}\cdot\tau)d\Omega \tag{10}$$

2.4 Computational setup

The numerical tests are carried out in a three-dimensional (3D) numerical wave tank (NWT) (Fig. 1). The numerical results are compared with the experimental results by Chakrabarti et al. (1997). The NWT is 31 m long, 1.8 m high and 0.40 m wide. The still water level over the horizontal bottom is $d = 1.01$ m. The numerical setup employs a vertical cylinder with an uniform diameter $D = 0.046$ m and is placed at $x = 13.41$ m. Five wave gauges are placed at $x =$ -2.00 m (W1), 5.00 m (W2), 11.59 m (W3), 13.41 m (W4), 15.59 m (W5) to measure the free surface elevations; three velocity probes are placed at the free surface with x and y coordinates as: P1 (11.59 m, 0.20 m), P2 (13.41 m, 0.15 m), P3 (15.59 m, 0.20 m) to measure the particle velocities. The irregular waves are generated using the Bretschneider spectrum. The goal of the paper is to first validate the numerical model against the experimental data before performing extensive numerical analysis. The waves in the experiments by Chakrabarti et al. (1997) were generated using the Bretschneider spectrum. Therefore, the authors have used the same wave spectrum to simulate the experimental waves in the numerical model. The numerical simulations for the validation of the numerical model are conducted for 2 different cases as listed in Table 1. The computations are conducted on the supercomputer which is based on the Intel Xeon E5–2670 processor with 2.6 GHz speed and a memory of 2 GB per core. Furthermore, 256 processors are used for the present simulations.
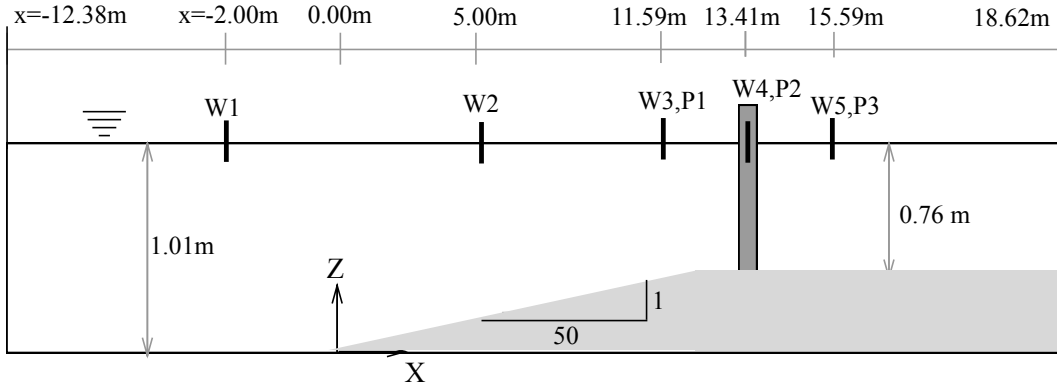
Figure 1: Numerical wave tank setup to simulate the experiments by Chakrabarti et al. (1997)

Cases	Input	Significant wave height, H_s (m)						Peak period, T_p (s)	Grid size, dx (m)	Significant force, F_s (N)	
		W3		W4		W5					
		Exp	Num	Exp	Num	Exp	Num			Exp	Num
		0.459	0.381	0.468	0.402	0.411	0.348		0.05	–	14.54
Case 1	0.457	0.459	0.422	0.468	0.411	0.411	0.353	2.9	0.025	–	19.92
		0.459	0.441	0.468	0.446	0.411	0.382		0.01	–	20.12
		–	0.263	–	0.276	–	0.221		0.05	17.04	12.95
Case 2	0.330	–	0.284	–	0.295	–	0.241	2.9	0.025	17.04	16.89
		–	0.317	–	0.331	–	0.268		0.01	17.04	17.11

Table 1: List of cases for the validation of the numerical model with the experiments by Chakrabarti et al. (1997)

2.5 Grid convergence study for the wave free surface elevation and breaking irregular wave force

The grid convergence study is carried out for the free surface elevation and breaking irregular wave force in the NW. The numerical model is based on the Cartesian grid, which means that the mesh size is uniform in all directions ($dx = dy = dz$). For the free surface elevation, the numerical simulations are performed with a significant wave height $H_s = 0.457$ m and a peak period of $T_p = \frac{2\pi}{\omega_p} = 2.9$ s for three different grid sizes $dx = 0.05$ m (total number of mesh elements= 178,560), 0.025 m (total number of mesh elements= 1.4 million) and 0.01 m (total number of mesh elements= 22.3 million), as listed in the Table 1 (case 1). The wall time (CPU time) is around 10 hours with $dx = 0.05$ m, 70 hours with $dx = 0.025$m and 250 hours for each case with $dx = 0.01$ m. The simulations are run for 200 s of data. The local wave spectrum S_η at the wave gauges is normalised with respect to the incident wave spectrum, i.e.
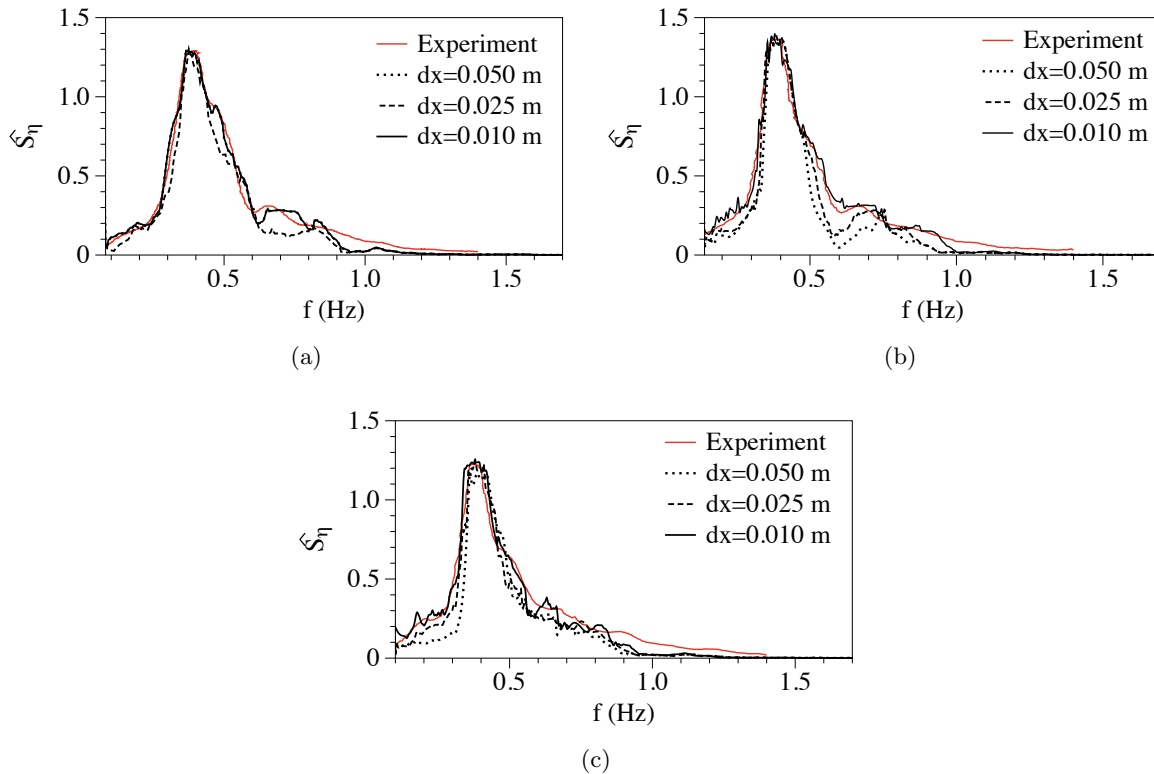
Figure 2: Comparison of the normalised numerical and experimental wave spectrum $\hat{S}_\eta$ with different grid sizes dx for case 1 ($H_s = 0.457$ m, $T_p = 2.9$ s) at a) W3 ($x = 11.59$ m) b) W4 ($x = 13.41$ m) c) W5 ($x = 15.59$ m)

$$\hat{S}_\eta(f) = \frac{S_\eta(f)}{S(f)} \tag{11}$$

where $f = \frac{2\pi}{\omega}$.

Fig. 2 presents the comparison of the normalised numerical and experimental wave spectrum $\hat{S}_\eta$ with different grid sizes dx for case 1 at W3, W4 and W5. It appears that the numerical results with $dx = 0.05$ m and 0.025 m underestimate the wave energy content at W3. The value of the primary spectral peak at $f = 0.34$ Hz is in agreement with the experiments, but the spectral values in the higher frequencies (0.6-1.2 Hz) is not represented correctly at these grid sizes. This is due to the lack of sufficient cells per wavelength. The computed H_s is lower than the experimental values by 17 % and 8.1 % for the cases with dx = 0.05 m and 0.025 m, respectively (Fig. 2a).

The results with $dx = 0.01$ m are in reasonable agreement with the experimental data for most of the frequency range. The difference between the experimental and numerical value of H_s reduces to 3.9 %. When the waves reach the cylinder, some of the shoaled waves attain their maximum heights due to the sloping seabed after which they break. A few waves continue to shoal (waves which have not reached their maximum heights), as computed at the wave gauge

located besides the cylinder (W4). At W4, the computed H_s is lower than the experimental values by 14.1 % and 12.2 %, for the cases with $dx = 0.05$ m and 0.025 m, respectively. The difference between the experimental and numerical value of H_s reduces to 4.7 % at $dx = 0.01$ m (Fig. 2b). The wave gauge located behind the cylinder (W5) measures the waves which have already broken and lost most of their energy. Thus, the spectral values at W5 is lower than at W4 due to the loss of wave energy. The computed H_s is lower than the experimental values by 15.3 % and 14.1 %, for the cases with $dx = 0.05$ m and 0.025 m, respectively. The difference between the experimental and numerical value of H_s reduces to 7.1 % at $dx = 0.01$ m. The values of the numerical wave spectrum at W5 is lower than the experimental values in the frequency range from 0.9 Hz to 1.4 Hz (Fig. 2c). Even though, the numerical results for $dx = 0.01$ m represent most of the wave energy and frequencies well (0-0.9 Hz) with a low uncertainty (2.2 %) , but it should be noticed that the difference between the experimental and numerical values in the high frequency range (0.9 Hz to 1.4 Hz) is around 42 % at all wave gauges. The number of elements per wavelength corresponding to waves at peak frequency are around 800, which are enough to model waves at these frequencies correctly resulting in a good agreement at the peak frequencies. However, at higher frequencies (around 0.9 Hz or more), the number of elements per wave length is about 200 or less. This explains the discrepancies in the high frequency ranges, as a further refined grid size is required in order to capture them accurately. A very refined grid size would increase the computational costs manifolds which are beyond the scope of the present study. But, since the energy content is quite low (less than 4 %) at these frequencies, it can be concluded that overall, the numerical results with $dx = 0.01$ m simulates the experimental waves with reasonable accuracy, i.e., the primary and secondary spectral peaks are well represented (Fig. 2). In general, the spectral evolution of the waves during the transformation processes like wave shoaling, wave breaking and wave decomposition post-breaking is reproduced well at $dx = 0.01$ m.

After the numerical model is validated for the free surface elevation, a grid convergence study is performed for the total force spectrum. The simulations are performed with $H_s = 0.33$ m and $T_p = 2.9$ s with three different grid sizes $dx = 0.05$ m, 0.025 m and 0.01 m, as listed in the Table 1 (case 2). Here, horizontal component of the total force is considered, since it is dominant over the other two directions. Fig. 3a presents the grid refinement study in terms of normalized force spectrum $\hat{S}_F$ on the vertical cylinder. Further, the numerical wave spectrum at this location of wave impact (W4 ; $x = 13.41$ m) can be seen in Fig. 3b.

$$\hat{S}_F = \frac{S_F}{T_p(\rho g(\pi D^3/4))^2} \tag{12}$$

The force spectrum has a primary peak at $f = 0.36$ Hz for the results with all grid sizes. The peak of the numerical force spectrum is lower by 19.5 % and 9.5 % for $dx = 0.05$ m and 0.025 m, respectively, than the corresponding experimental peak value. This difference reduces to less than 1 % for $dx = 0.01$ m. The value of the numerical significant wave force F_s is lower by 24.0 %, 8.1 % and 0.6 % for $dx = 0.05$ m, 0.025 m and 0.01 m, respectively, than the experimental significant wave force F_s. The secondary peak at $f = 0.57$ Hz is in good agreement with experimental results for $dx = 0.025$ m and 0.01 m. The primary spectral peak in the force spectrum corresponds to the peak frequency of the irregular wave train. The secondary peak is due to the interaction of the decomposed wave components with the cylinder, i.e., the higher frequency components are generated because of the wave energy redistribution towards shorter waves (higher frequencies) during wave breaking (Tian et al.,
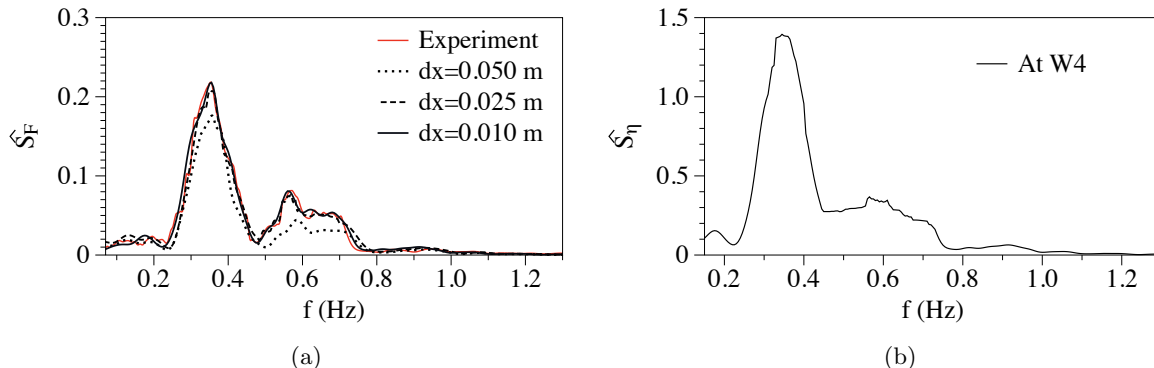
Figure 3: Normalised spectra for case 2 ($H_s = 0.330$ m, $T_p = 2.9$ s) (a) experimental and numerical force spectrum $\hat{S}_F$ with different grid sizes dx (b) Numerical wave spectrum at this location; at W4 ($x = 13.41$ m)

2011). Fig. 3b demonstrates the numerical wave spectrum besides the cylinder at W4. The wave forces are measured with a reasonable accuracy at $dx = 0.025$ m, but the numerical results with $dx = 0.01$ m gives more detailed information about the flow properties. Thus, the grid size of 0.01 m is chosen for the further simulations. The time-step is calculated based on the CFL number in the numerical model (Bihs et al., 2016a).

3 Investigation of breaking irregular wave forces and associated parameters

3.1 Numerical setup

In order to investigate the hydrodynamic properties of irregular breaking waves and the associated breaking wave forces for different spectral wave steepnesses, seven different configurations are performed. The spectral wave steepness for irregular waves is defined by:

$$s = \frac{2\pi H_{so}}{gT_p^2} \tag{13}$$

In the first four cases (A1-A4), the wave steepness is varied by modifying the incident offshore significant wave height H_{so}, while maintaining the peak period T_p. In cases B1-B3, the wave steepness is changed by varying the peak period T_p, while keeping the incident significant wave height H_{so} the same. The simulation cases are listed in Table 2.

3.2 Wave height transformation

The changes in the irregular free surface elevation for irregular waves can be investigated with the wave energy spectrum. When waves approach from deep water to shallow water, the characteristics of the irregular wave group such as wave energy, wave height and wave length change due to the varying water depth; their group velocity decreases. In order to keep the energy flux constant, the decrease in the group velocity is compensated by an increase in the

Sim. No.	Significant wave height H_{so} (m)	Peak period T_p (s)	Spectral steepness s	Significant force F_s (N)
A1	0.30	2.9	0.023	14.34
A2	0.50	2.9	0.038	26.23
A3	0.55	2.9	0.042	32.21
A4	0.60	2.9	0.046	35.51
B1	0.55	2.0	0.088	24.91
B2	0.55	2.5	0.056	30.64
B3	0.55	3.5	0.029	22.08

Table 2: Simulation cases for the study of breaking irregular wave forces on a cylinder mounted on an impermeable slope

energy density, i.e. the wave height. Figs. 4 and 5 present the computed free surface profile with velocity variation during the wave breaking process in the irregular wave train for cases A4 ($s = 0.046$) and B2 ($s = 0.056$), respectively. For case A4, the waves start shoaling near the toe of the slope and continue to shoal up to the breaking point (Figs. 4a and 4b). The wave crest overturns and collapses at the cylinder resulting in the breaking wave impact on the cylinder (Figs. 4c and 4d). After wave breaking, a chute-like downstream jet is formed as observed in Figs. 4e and 4f. Most of the waves in the irregular wave train for case A4 break near the cylinder, Fig. 4 shows the breaking process for one such wave in the irregular wave train. The breaking waves exert higher wave loads due to the collapsing tip of the wave crest and the large amount of water impacting the cylinder. For case B2, the wave steepness is relatively larger ($s = 0.056$) implying that most of the wave components attain the breaking limit before impacting the cylinder and that they break in the vicinity of the cylinder (Fig. 5). On further increasing the wave steepness (case B1, $s = 0.088$), the wave non-linearity increases due to a larger number of steep wave components. Consequently, the higher-order wave-wave interactions become significant and generate very steep wave crests, and waves break further offshore and away from the cylinder in this case (Banner and Peregrine, 1993). Therefore, it is important to investigate the complex wave height transformations around the cylinder for a better understanding of the breaking irregular wave forces.

Fig. 6 presents the variation in the normalised wave spectrum $\hat{S}_\eta$ for breaking irregular waves versus frequency f for (a) case A1 (low spectral wave steepness $s = 0.023$) (b) case B1 (high spectral wave steepness $s = 0.088$). For case A1 (Fig. 6a), the wave gauge located far away from the cylinder (W2), the second spectral peak is not very pronounced. When waves propagate further, the wave gauge located before the cylinder (W3) exhibits two small spectral peaks around the peak frequency region. This might be attributed further to the wave shoaling (Elgar et al., 1997). This leads to a transfer of the spectral peak energy ($f = 0.321$ Hz) to slightly higher frequencies ($f = 0.417$ Hz). This phenomenon contributes to an additional peak in the peak frequency region. Another reason for this could be due to the interaction between waves and structure. When the waves propagate further, more waves in the wave train attain their maximum wave heights and break in the vicinity of the cylinder (W4). However, the difference between the spectral peaks at W4 and W3 is very small (4.6
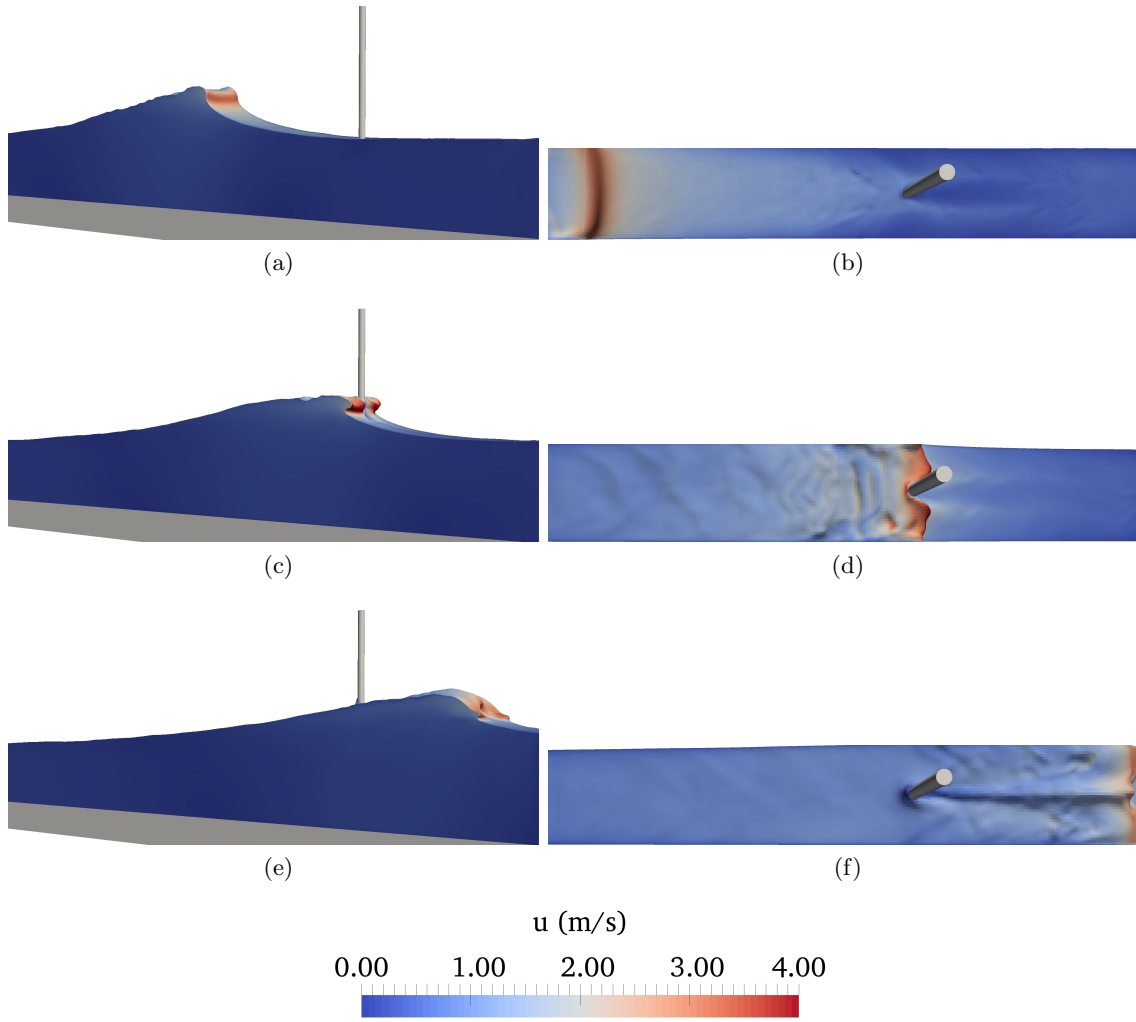
Figure 4: Computed wave profile during wave breaking with the velocity variation on the cylinder for case A4 ($H_{so} = 0.60$ m, $T_p = 2.9$ s, $s = 0.046$) at $t =$ (a) 75.9s (isometric-view) (b) 75.9s (top-view) (c) 76.3s (isometric-view) (d) 76.3s (top-view) (e) 76.5s (isometric-view) (f) 76.5s (top-view)

%) which means that only a few waves break in the irregular wave train and they attain their breaking wave height at the cylinder. For the wave gauge located after the cylinder (W5), both spectral peaks are reduced. The primary spectral peak is reduced by 11.2 % (Fig. 6a). This is due to the loss of wave energy during the wave breaking process and the interaction with the cylinder. In the case of higher wave steepness (case B1), the primary spectral peak is lower than for case A1. The spectrum at W2 for this case is larger than at W3, because most of the waves have already shoaled at this point, and on further shoaling , they start to break and have lost most of their energy before reaching W3 (Fig. 6b). However, the wave spectrum still contains some shoaled waves which have not yet broken. The spectral peak values at W3 and W4 (beside the cylinder) reduce to less than 1 due to the large number of breaking waves

Aggarwal, A. et al., 2019

(a)

(b)

(c)

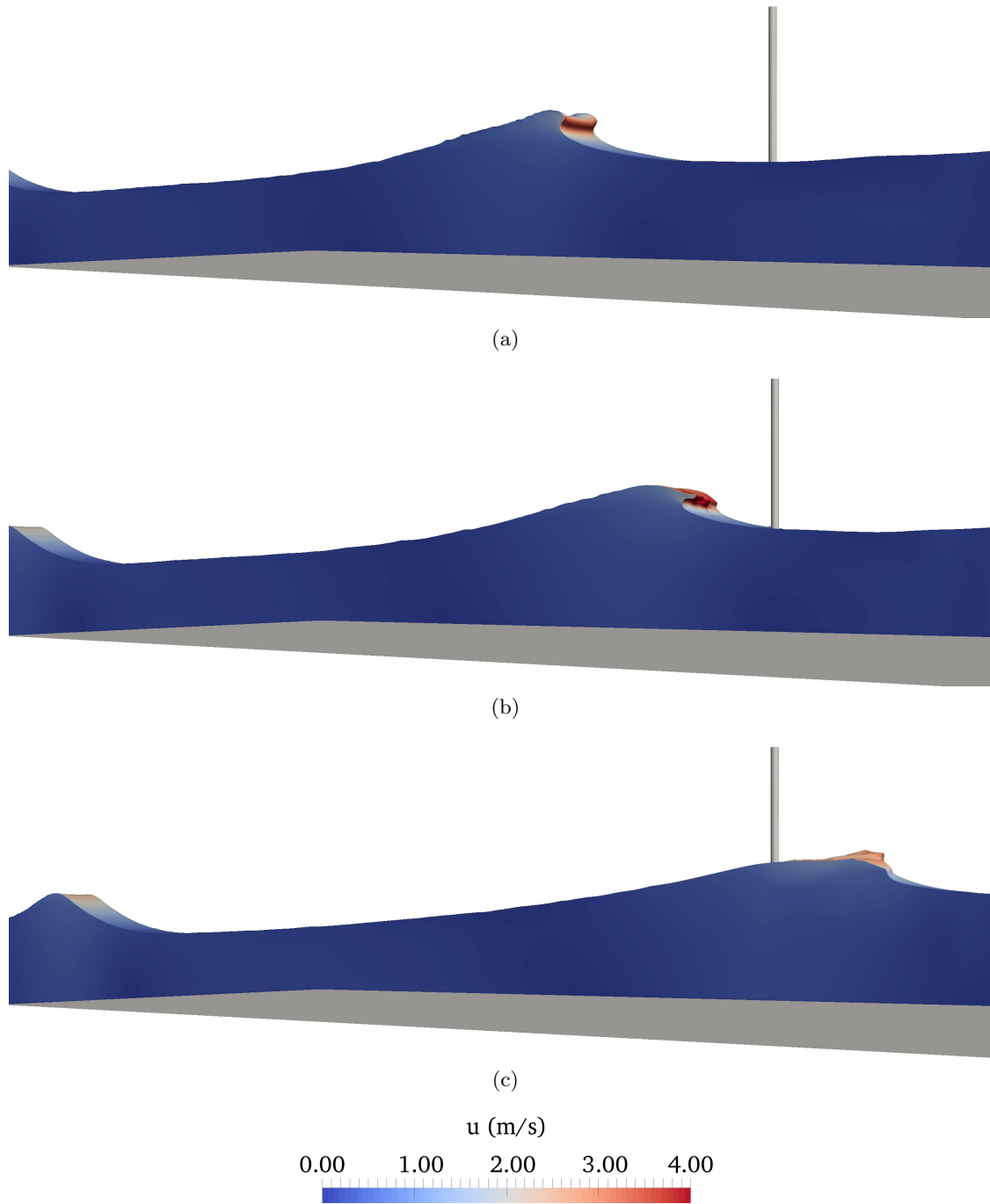u (m/s)

0.00   1.00   2.00   3.00   4.00

Figure 5: Computed wave profile during wave breaking with the velocity variation in the vicinity of the cylinder for case B2 ($H_{so} = 0.55$ m, $T_p = 2.5$ s, $s = 0.056$) at $t =$ (a) 53.3s (b) 53.45s (c) 53.85s

in the wave train. The offshore wave energy dissipation leads to reduced magnitude of the wave impact forces on the cylinder. After the waves propagate towards the lee side of the

cylinder (W5, wave gauge located after the cylinder), the spectral peak is reduced further.

(a) (b)
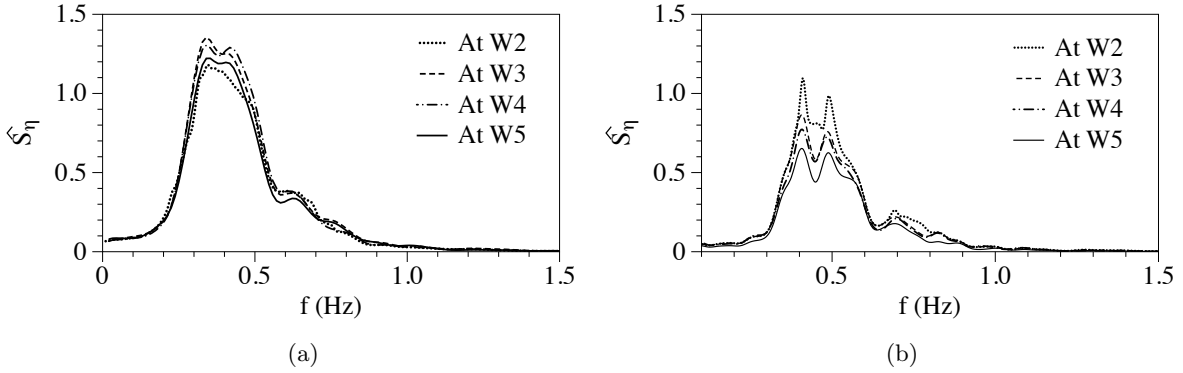
Figure 6: The normalized numerical wave spectrum $\hat{S}_\eta$ versus frequency f at different wave gauge locations for (a) case A1 ($H_{so} = 0.30$ m, $T_p = 2.9$ s, s=0.023) (b) case B1 ($H_{so} = 0.55$ m, $T_p = 2.0$ s, s=0.088). W3 is at $x = 11.59$ m, W4 is at $x = 13.41$ m and W5 is at $x = 15.59$ m.
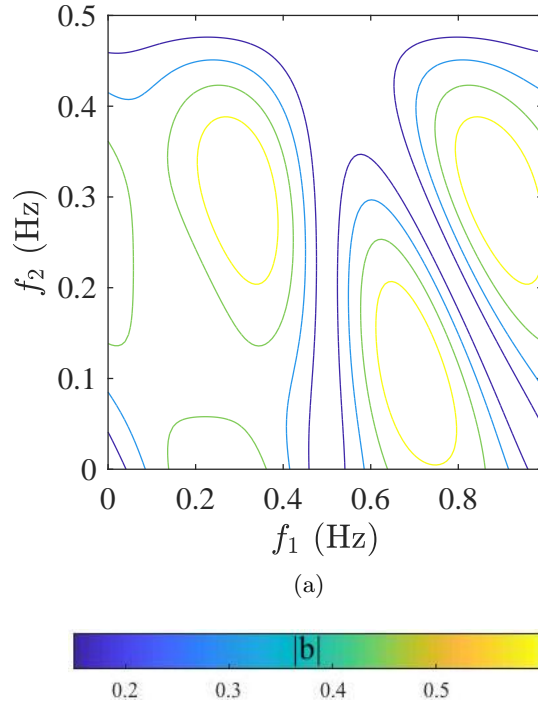

(a)

Figure 7: Bicoherence estimate for numerical free surface elevation for case A1 ($H_{so} = 0.30$ m, $T_p = 2.9$ s, $f_p = 0.35$ Hz, s=0.023) at W4 ($x = 13.41$ m).

Further, a bispectrum analysis is performed for case A1 ($H_{so} = 0.30$ m, $T_p = 2.9$ s, $f_p = 0.35$ Hz, s=0.023) to understand the couplings between different frequencies during wave shoaling and wave breaking processes. Bound waves generated as a result of wave nonlinearity

play an important role in this process. The present study uses the procedure similar to that of Elgar and Guza (1985) for the bispectrum analysis with 95 % significance levels for the normalization of bicoherences. Fig. 7 presents the bicoherence amplitude ($\|b\|$) spectrum for case A1. It indicates nonlinear couplings between different modes of the power spectrum shown in Fig. 6a. The bicoherence shows a strong coupling between the peak frequencies (f_p, f_p). A strong coupling is further observed between f_p and at about $2f_p$, also strong coupling is observed between lower frequencies ($< f_p$) and higher frequencies ($> f_p$). This means that the waves at these frequencies are bound waves. In addition, there is relatively weak coupling between f_p and higher-frequencies due to the nonlinear wave shoaling and wave breaking processes which behave as relatively free waves. Thus, the bispectrum shown in Fig. 7 illustrates the coupling between different frequency ranges and the transfer of wave energy from the peak frequency to larger frequencies.

Fig. 8 presents the distribution of the normalized local significant wave height (H_s/H_{so}) versus the distance along the wave tank (x) for (a) cases A1-A4 (same T_p, different H_{so} and (b) cases B1-B3 (different T_p, same H_{so}). The wave height becomes $1.42H_{so}$) for case A4 ($s=0.046$) compared to case A1 ($s = 0.023$), where H_s/H_{so} is 1.31 at the wave gauge before the cylinder (W3). For cases A4 and A1, the wave height is $1.28H_{so}$ and $1.36H_{so}$, respectively at the wave gauge located besides the cylinder (W4). The waves with lower spectral wave steepness have a higher H_s/H_{so} ratio due to the onshore wave breaking at relatively shallower water depths. Since the incident wave energy in case A4 is much larger compared to case A1, the breaking wave forces in case A4 are larger than in case A1, even though the waves lose a higher amount of wave energy in case A4 after offshore wave breaking. For the cases with the same H_{so} and different T_p (cases A3, B1 , B2 and B3), a similar behaviour is observed. In the case when the wave train is dominated by the shorter waves (case B1, $s = 0.088$), H_s/H_{so} attains its maximum value at $x = 5$ m (W2). The waves lose 9.8 % of their wave energy when they reach the cylinder (at W3) compared to the energy at W2. This is
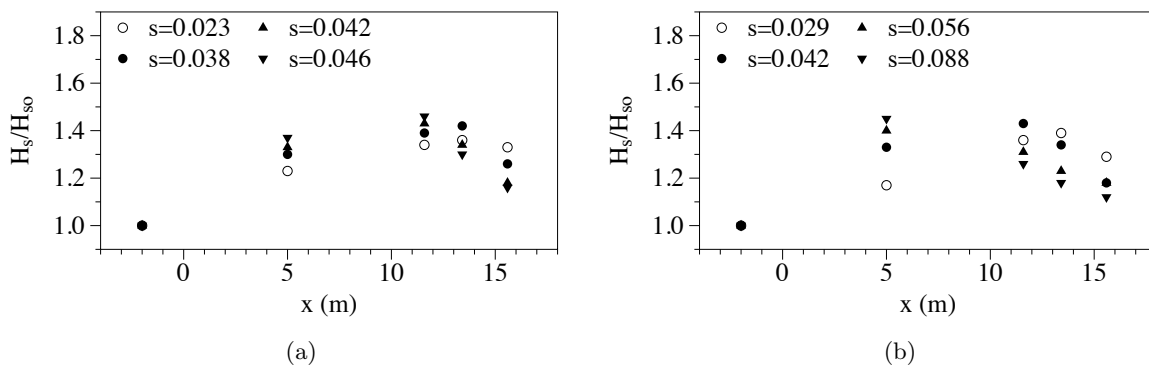

Figure 8: The normalized significant wave height H_s/H_{so} versus the distance along the wave tank for (a) cases A1 (s=0.023), A2 (s=0.038), A3 (s=0.042) and A4 (s=0.046) (b) cases A3 (s=0.042), B1 (s=0.088), B2 (s=0.056) and B3 (s=0.029).

due to the wave breaking at larger water depths. The rate at which the waves lose energy is higher in the cases with larger wave steepness s. The irregular wave train with larger s has

a higher number of individual waves which attain their breaking limit farther offshore. The wave breaking location and the number of breaking wave components in the irregular wave train are important factors in determining the magnitude and properties of the breaking wave forces.

3.3   Energy level evolution

This section demonstrates the energy transfer between the different frequency ranges of the wave spectrum by tracking the wave energy levels at different frequency ranges during the wave shoaling and wave breaking processes. Five different frequency ranges of the wave spectrum are considered: spectral peak region ($f/f_p = 0.9$-1.1, E_1), above-peak region ($f/f_p = 1.2$-1.5, E_2), higher-frequency region ($f/f_p = 1.5$-2.5, E_3), low frequency range ($f/f_p = 0.5$-0.9, E_4) and significantly high frequency region ($f/f_p = 2.5$-5, E_5). These energy levels are non-dimensionalised with the total incident wave energy E_0 near the wave generation boundary. The total wave energy at each wave gauge is computed by integrating the wave spectrum with wave components of frequencies lower than $5f_p$. This is similar to the methodology used by Tian et al. (2011) to investigate the energy transfer for breaking focused wave groups. Fig. 9 presents the variation of the energy levels at different frequency ranges versus the normalized distance in the NWT. As the waves propagate over the slope for case A1 ($H_{so} = 0.30$ m, $T_p = 2.9$ s, s=0.023), the energy reduces from both regions E_1 (spectral peak region) and E_4 (low frequency range) due to wave shoaling, and this energy is transferred to the above-peak region E_2 as noticed by an increase in E_2 (Fig. 9a). Moreover, the energy during the wave shoaling process in the high-frequency regions E_3 increases, while E_5 first reduces and then increases. After breaking (at $x/L_s = 0.82$), the energy from the spectral peak region E_1 is significantly reduced (43 %) compared to the energy in E_1 before the slope ($x/L_s = -2$). This is due to the energy dissipation during breaking and energy transfer towards E_2 and E_3, as noticed by the increase in their energy levels by almost 42 % and 33 %, respectively, after breaking. The energy levels in the significantly high frequency range E_5 are not affected much. Furthermore, total wave energy is reduced by around 20 % compared to total incident wave energy. For case B1 ($H_{so} = 0.55$ m, $T_p = 2.0$ s, s=0.088), a similar behaviour is observed (Fig. 9b). However, wave breaking occurs at larger water depths for this case, since the energy dissipation from the spectral peak E_1 for case B1 occurs earlier (after $x/L_s = 0.31$) and some of the energy is transferred to the higher-frequencies in E_2 and E_3. Total energy is reduced by more than 30 % compared to total incident energy after wave breaking for this case.

3.4   Breaking irregular wave forces

Breaking waves exert large impact forces on the cylinder due to the overturning wave crest with a water jet impacting the cylinder. Due to this, the breaking irregular wave forces are larger in magnitude and more complex in nature compared to the non-breaking irregular wave forces. Time-series for horizontal wave-induced impact loads for cases A1 ($s = 0.023$) and A4 ($s = 0.046$) is also shown in Figs. 10a and 10b, respectively. The wave force is highly irregular and random. Fig. 9 presents the variation of the normalised force spectrum $\hat{S_F}$ versus frequency f for (a) cases A1-A4 (different H_{so}, same T_p) (b) case A3 and cases B1-B3 (same H_{so}, different T_p). In general, when T_p is kept constant and H_{so} is varied, the
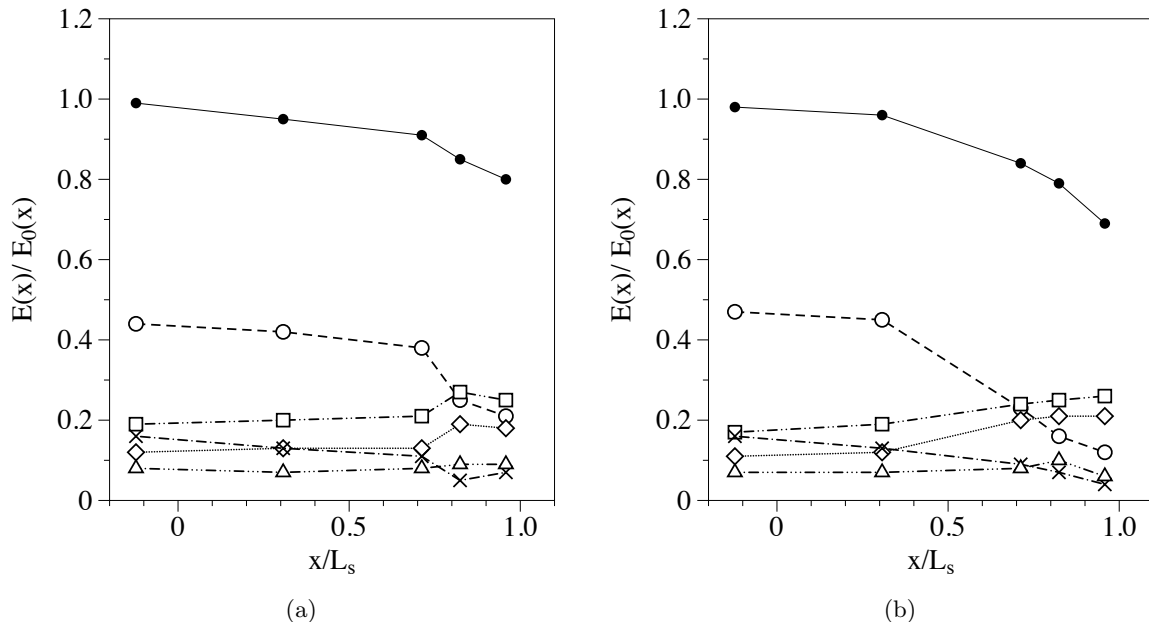
Figure 9: The energy levels versus the normalized distance in NWT for (a) case A1 ($H_{so} = 0.30$ m, $T_p = 2.9$ s, s=0.023) (b) case B1 ($H_{so} = 0.55$ m, $T_p = 2.0$ s, s=0.088). Open circles represent $E_1(x)/E_0(x)$; squares represent $E_2(x)/E_0(x)$; rhombus represent $E_3(x)/E_0(x)$; crosses represent $E_4(x)/E_0(x)$; triangles represent $E_5(x)/E_0(x)$. E_1 for spectral peak region ($f/f_p = 0.9$-1.1), E_2 for above-peak region ($f/f_p = 1.2$-1.5), E_3 for higher-frequency region ($f/f_p = 1.5$-2.5), E_4 for low frequency range ($f/f_p = 0.5$-0.9) and E_5 for significantly high frequency region ($f/f_p = 2.5$-5).

value of the primary spectral force peak increases as the spectral wave steepness s increases (Fig. 10c). The multiple secondary peaks are observed in the higher frequencies which might be attributed to the shorter wave components generated during the wave breaking process. However, when the wave steepness increases such that more wave components in the irregular wave train break farther offshore (before the cylinder), the increase in the peak value of the force spectrum is quite small due to the offshore dissipation in wave energy. The normalised spectral force peak is further increased for case A2 ($s = 0.038$) and case A3 ($s = 0.042$). By further increasing the wave steepness (case A4, $s = 0.046$), the increase in the primary spectral peak is very small (3.3 %) and the secondary spectral peak is slightly reduced (Fig. 10c). Most of the waves in this irregular wave train break at the cylinder (Fig. 4). Due to the larger incident wave energy (higher incident H_{so}) and the pronounced wave breaking at the cylinder, the breaking wave forces and consequently, the value of the primary spectral force peak is higher.

When the spectral wave steepness is changed by changing T_p (keeping H_{so} constant), the value of the primary spectral peak is highest in case A3 ($s = 0.042$). The incident wave energy is the same in these cases (due to same incident H_{so}), but the wave breaking location shifts farther offshore (away from the cylinder), when spectral wave steepness s is increased (by reducing T_p) (Fig. 10d). Since most of the energy dissipation occurs offshore (Fig. 5),

16

the magnitude of the breaking wave forces on the cylinder is reduced. In case B1, the wave steepness is quite high ($s = 0.088$), but the value of the spectral force peak is reduced as compared to case A3. Here, in addition to the depth-induced wave breaking, the role of wave-wave interactions becomes important. The irregular wave train with the larger incident H_{so} contains a larger number of wave components with larger wave steepness. The wave breaking is also initiated by the steeper wave components generated as a result of wave-wave interactions. Due to a large number of wave components breaking farther offshore, the waves lose a significant amount of wave energy before reaching the cylinder and exert relatively lower wave forces.

The values of the significant breaking wave force F_s is computed from the wave force spectra as shown in Table 2. Fig. 11 presents the variation of the significant wave force F_s versus wave steepness s (cases A1-B3). As s increases, the value of the significant wave force F_s increases up to a certain point (until $s = 0.046$). By increasing s further, a major portion of the waves in the irregular wave train starts to break at larger water depths (far before the cylinder) and a reduction in F_s is observed.
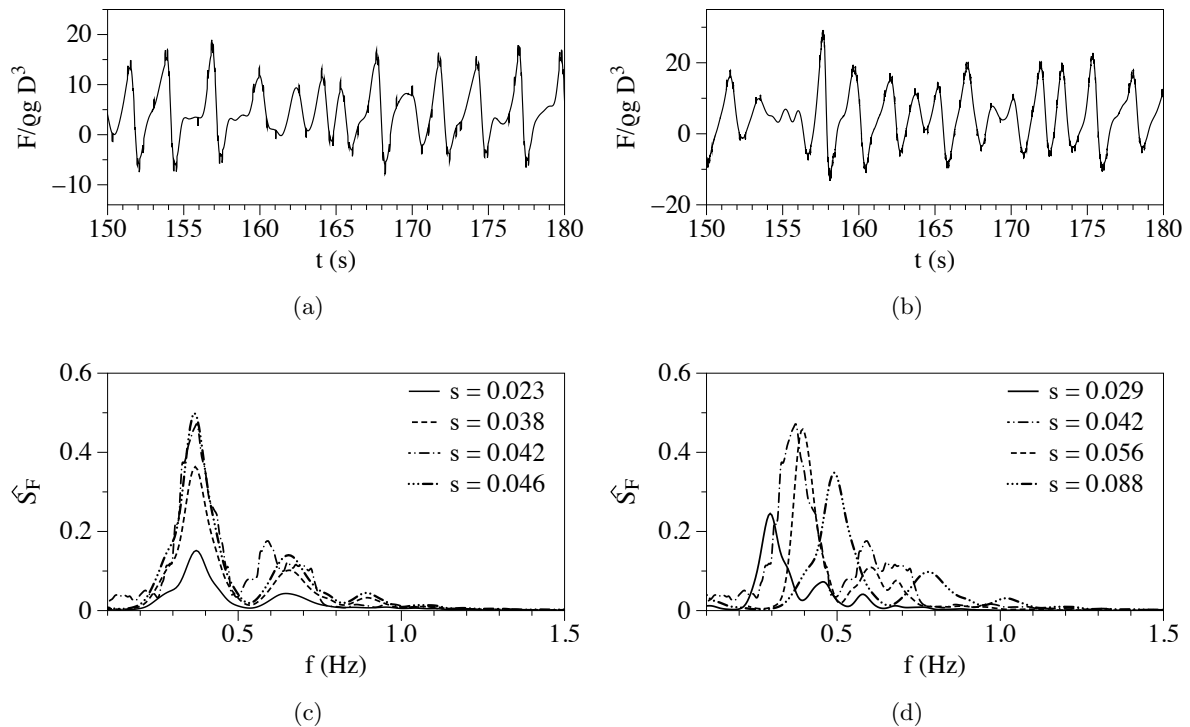

Figure 10: The normalized numerical force results (a) force time-series for case A1 (s=0.023); (b) force time-series for case A4 (s=0.046); (c) spectrum $\hat{S_F}$ versus frequency for cases A1 (s=0.023), A2 (s=0.038), A3 (s=0.042) and A4 (s=0.046); (d) spectrum $\hat{S_F}$ versus frequency for cases A3 (s=0.042), B1 (s=0.088), B2 (s=0.056) and B3 (s=0.029).
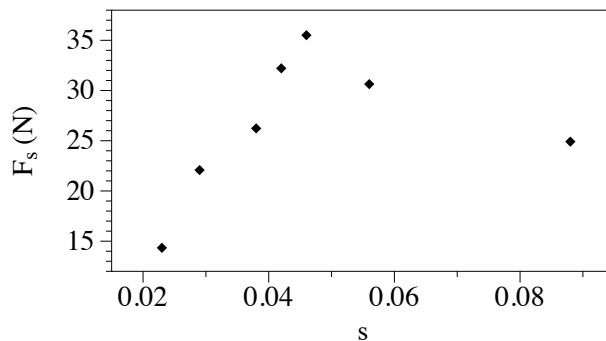
Figure 11: The significant wave force F_s versus spectral wave steepness for cases A1 (s=0.023), A2 (s=0.038), A3 (s=0.042), A4 (s=0.046), B1 (s=0.088), B2 (s=0.056) and B3 (s=0.029).

3.5 Free surface elevation skewness and spectral bandwidth

When the waves undergo transformation during the propagation from deep to shallow water, the skewness of the free surface and the spectral bandwidth of the irregular wave train also change. The skewness of the free surface elevation η is quantified as (Goda, 2010):

$$\beta = \frac{1}{\eta_{rms}^3} \frac{1}{N} \sum_{i=1}^{N} (\eta_i - \bar{\eta})^3 \tag{14}$$

where, $\bar{\eta}$ is the mean free surface elevation and η_{rms} is the root-mean-square (rms) value. The spectral bandwidth (ν) is defined as (Longuet-Higgins, 1975) :

$$\nu^2 = \frac{m_0 m_2}{m_1^2} - 1 \tag{15}$$

where, m_n is the spectral moment:

$$m_n = \int_0^\infty \omega^n S(\omega) d\omega; n = 0, 1, 2....... \tag{16}$$

Fig. 12 presents the distribution of the skewness (β) versus the distance in the wave tank (x) for (a) cases A1-A4 and (b) cases B1-B3. In general, the skewness increases up to the breaking point and it is nearly invariant after breaking. For cases A1-A4 (same T_p), the skewness β for the waves with small s (compared with the waves with larger s) is always higher both at and after breaking. The skewness becomes 0.035 at the cylinder (W4) and 0.037 after the cylinder (W5) (post wave breaking) for case A1 ($s = 0.023$). A similar behaviour is observed for cases B1-B3. For a given offshore significant wave height H_{so}, the wave components with lower T_p break more offshore and have a lower skewness compared to the cases with larger T_p. The wave components with lower s possess a larger β because these wave components are relatively longer and travel faster over the slope and undergo more deformation (Goda, 2010). The skewness influences the breaking wave forces for irregular waves. The non-linear wave components contribute towards the higher-order wave forces in the force spectrum. Fig. 14a presents the significant wave force F_s versus the skewness β

computed at the wave gauge located besides the cylinder (W4). The value of F_s increases as the skewness β increases up to a certain value (0.015) and decreases afterwards.
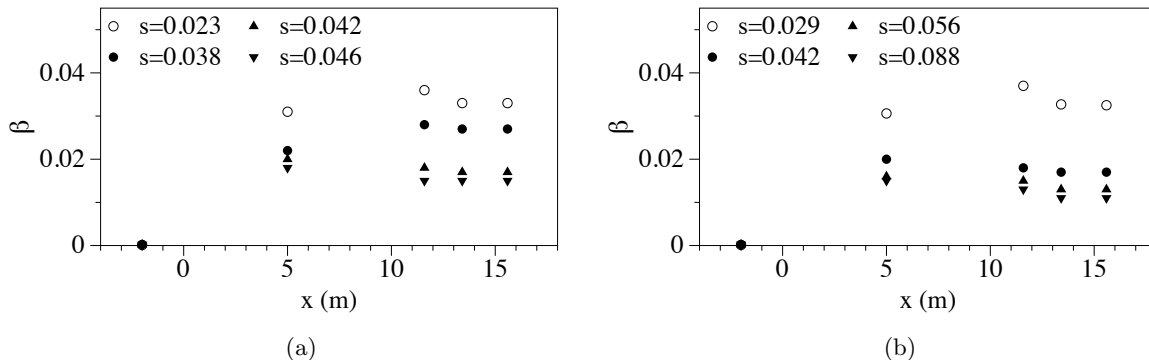

Figure 12: The skewness β versus the distance along the wave tank for (a) cases A1 (s=0.023), A2 (s=0.038), A3 (s=0.042) and A4 (s=0.046) (b) cases A3 (s=0.042), B1 (s=0.088), B2 (s=0.056) and B3 (s=0.029).

Fig. 13 presents the variation of the normalized bandwidth $\hat{\nu}$ versus the distance along the wave tank (x) for (a) cases A1-A4 (same T_p, different H_{so}) and (b) cases B1-B3 (different T_p, same H_{so}). The bandwidth is normalized with the offshore bandwidth value at W1 (before wave transformation). In general, the spectral bandwidth increases until the wave components (both non-breaking and breaking) attain their maximum heights during shoaling. For all the cases A1-B3, the spectral bandwidth $\hat{\nu}$ for waves with larger s increases up to the wave breaking location, and then it decreases in the surf zone. The energy loss takes place during wave breaking as energy from the peak regions is redistributed to the shorter wave components and the wave spectrum becomes narrower. The distribution of the wave energy over the frequency range changes during the breaking process as quantified by $\hat{\nu}$. Fig. 14b presents the significant wave force F_s versus the normalized bandwidth $\hat{\nu}$ computed at the wave gauge located besides the cylinder (W4). In general, F_s increases as $\hat{\nu}$ increases. A larger bandwidth means that a larger amount of the non-linear energy transfer has taken place and a relatively larger number of wave components in the irregular wave train shoal to attain their breaking limits (Tian et al., 2011). After wave breaking has occurred, $\hat{\nu}$ decreases further due to energy dissipation (Figs. 13a and 13b). However, in some cases where the local wave energy is larger, the breaking F_s is larger even though the bandwidth is smaller (case B1, Fig. 14b). Therefore, the local wave energy and the breaking location are the most important factors in determining the significant wave forces. In general, the wave spectrum with a larger bandwidth exerts the larger breaking wave forces on the cylinder.
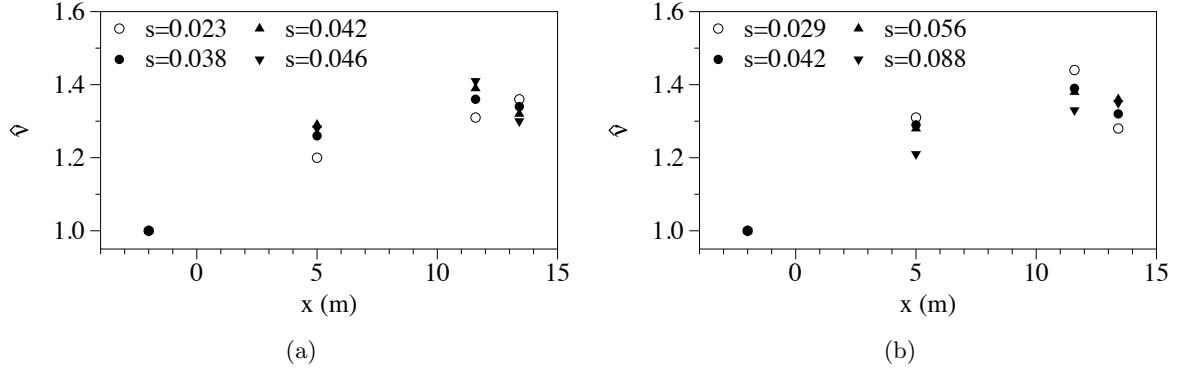
(a)

(b)

Figure 13: The normalized bandwidth $\hat{\nu}$ versus the distance along the wave tank for (a) cases A1 (s=0.023), A2 (s=0.038), A3 (s=0.042) and A4 (s=0.046) (b) cases A3 (s=0.042), B1 (s=0.088), B2 (s=0.056) and B3 (s=0.029).
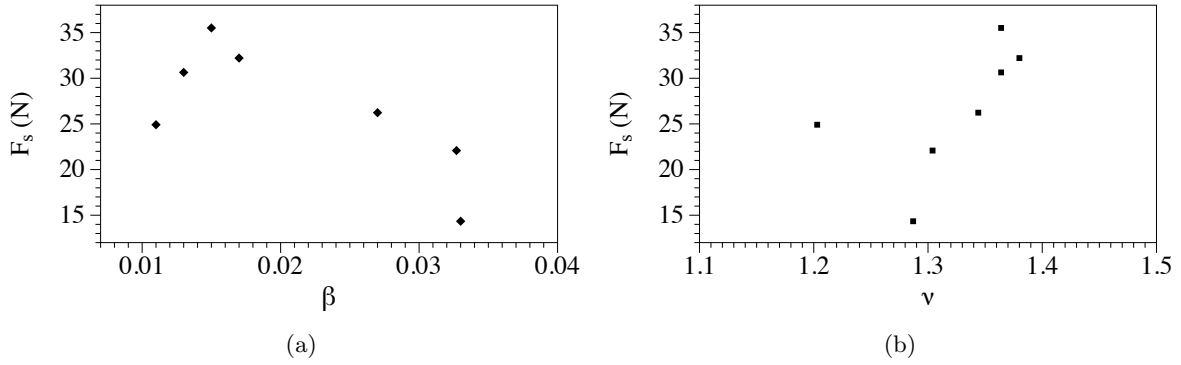

(a)

(b)

Figure 14: The significant wave force F_s at the wave gauge located besides the cylinder $W4$ (x = 13.41m) for cases A1 (s=0.023), A2 (s=0.038), A3 (s=0.042), A4 (s=0.046), B1 (s=0.088), B2 (s=0.056) and B3 (s=0.029) with (a) β (b) $\hat{\nu}$

3.6 Breaking wave characteristics

The breaking of regular waves can be defined by four types: spilling, plunging, collapsing and surging depending on the surf similarity parameter. The surf similarity parameter at breaking (ξ_b) is a function of the wave steepness at breaking (s_b) and the slope of the seabed (m) (Battjes, 1974).

$$\xi_b = \frac{m}{\sqrt{s_b}}; s_b = \frac{2\pi H_b}{gT^2} \tag{17}$$

$$\begin{cases} \xi_b < 0.4 & \text{Spilling} \\ 0.4 < \xi_b < 2.0 & \text{Plunging} \\ \xi_b > 2.0 & \text{Surging or Collapsing} \end{cases} \tag{18}$$

20

The breaker depth index (γ_b) and breaker height index (Ω_b) are two parameters used to investigate the breaking characteristics of waves. They are defined as:

$$\gamma_b = \frac{H_b}{d_b}; \Omega_b = \frac{H_b}{H_{so}} \tag{19}$$

where d_b is the depth at breaking, T is the zero-crossing period of individual waves at breaking, H_b is the local wave height at breaking and H_{so} is the offshore significant wave height.

Fig. 15 presents the breaker depth index (γ_b) (Fig. 15a) and the breaker height index (Ω_b) (Fig. 15b) versus the surf similarity parameter at breaking (ξ_b) for cases A1 and B1. For case A1 ($H_{so} = 0.30$ m, $T_p = 2.9$ s, s=0.023), it is observed that the trend lines for the scattered values of γ_b and Ω_b remain almost invariant with the change in ξ_b. Further, all of the waves break as spilling breakers and have values for Ω_b lower than 1, which means that none of the waves in the irregular wave train have a higher H_b than H_s during the shoaling process. The spilling breakers experience less reflections due to a lower ξ_b^2 (according to Battjes (1974), the reflection coefficient is directly proportional to ξ_b^2). The waves break more onshore at shallower water depths and experience more deformation. For case B1 ($H_{so} = 0.55$ m, T_p = 2.0 s, s=0.088), the trend of γ_b and Ω_b with ξ_b is similar to case A1. In this case, waves break farther offshore and experience more reflections from the slope for $\xi_b > 0.4$. The plunging breakers experience more reflections due to larger ξ_b^2. Moreover, the wave spectra with larger spectral wave steepness s undergo less deformation (Hajime and Kirby, 1992).
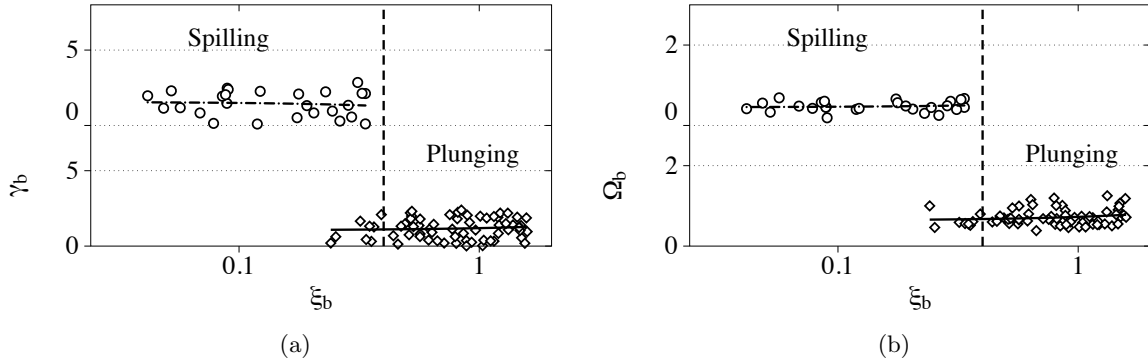

Figure 15: The (a) breaker depth index γ_b versus ξ_b; (b) breaker height index Ω_b versus ξ_b (logarithmic x-axis). Upper y-axis shows spilling breakers (case A1) and lower y-axis shows plunging breakers (case B1). Open circles represent case A1 ($H_{so} = 0.30$ m, $T_p = 2.9$ s, s=0.023); dashed black line is linear fit for case A1; rhombus for case B1 ($H_{so} = 0.55$ m, T_p = 2.0 s, s=0.088); solid black line is linear fit for case B1

Figs. 16 and 17 show the cumulative probabilities (CDF) for the normalized breaker indices $\hat{\gamma}_b$ and $\hat{\Omega}_b$, respectively, for cases A1 and B1. The breaker indices are normalized with their corresponding rms values. The figures show the numerical data together with the best fit of the Weibull distribution to the data. The Weibull PDF is given by:

$$p(x) = \frac{b}{a}(\frac{x}{a})^{b-1} exp\{-(\frac{x}{a})^b\} \tag{20}$$

where b is the shape parameter and a is the scale parameter; the best fit values of a and b are presented in Table 3.

Figs. 16a and 16b indicate that the Weibull distribution is an appropriate fit for the larger values of the breaker depth index $\hat{\gamma}_b$ for both spilling and plunging breakers (cases A1 and B1, respectively). For the irregular wave train dominated by the spilling breakers (case A1, $H_{so} = 0.30$ m, $T_p = 2.9$ s, s=0.023), the Weibull distribution can be taken to represent the $\hat{\gamma}_b$ data for $\hat{\gamma}_b > 0.3$. For plunging breakers (case B1, $H_{so} = 0.55$ m, $T_p = 2.0$ s, s=0.088), the Weibull distribution represents the data reasonably well for $\hat{\gamma}_b > 0.1$. The normalized breaker height index $(\hat{\Omega}_b)$ follows a trend similar to that for $\hat{\gamma}_b$ for case A1 (Fig. 17a). The Weibull distribution is a reasonable fit for spilling breakers for most of the $\hat{\Omega}_b$ values (case A1). For case B1 (plunging breakers), the Weibull distribution represents the data reasonably well for $\hat{\Omega}_b > 0.8$. (Fig. 17b), see Table 3 for details of the Weibull fit values.
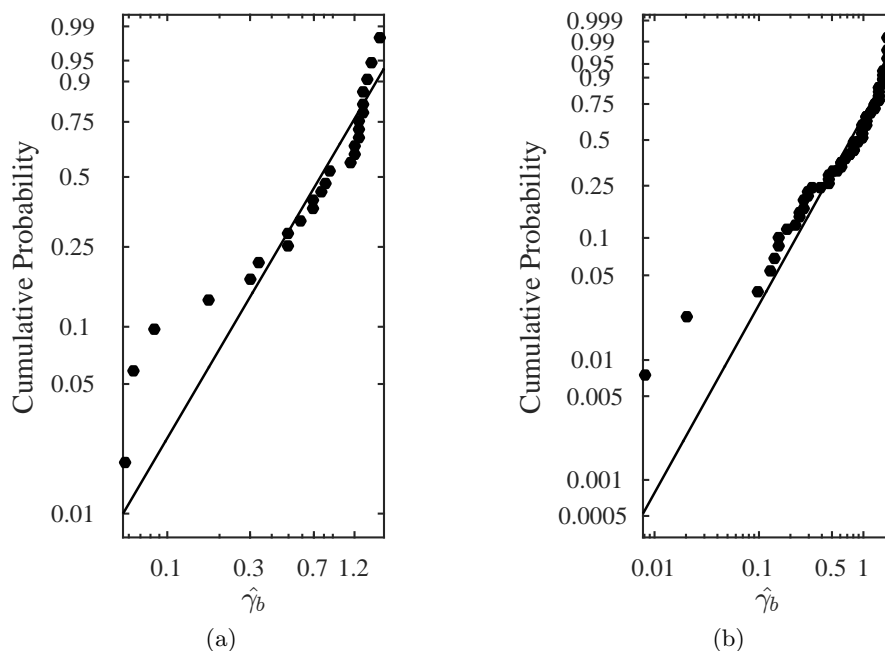

Figure 16: CDF fits in Weibull scale for the normalized breaker depth index $\hat{\gamma}_b$ for (a) case A1 ($H_{so} = 0.30$ m, $T_p = 2.9$ s, s=0.023) (b) case B1 ($H_{so} = 0.55$ m, $T_p = 2.0$ s, s=0.088). Open circles for numerical data; solid black line for Weibull fit (for details of the CDF fits, see Table 3)

3.7 Geometric properties of wave profile at breaking

During the breaking process, the waves become more steep and asymmetric. The present study investigates further the geometric properties of the wave profile at breaking by using the steepness and asymmetry parameters (Fig. 18) defined by Kjeldsen and Myrhaug (1978).

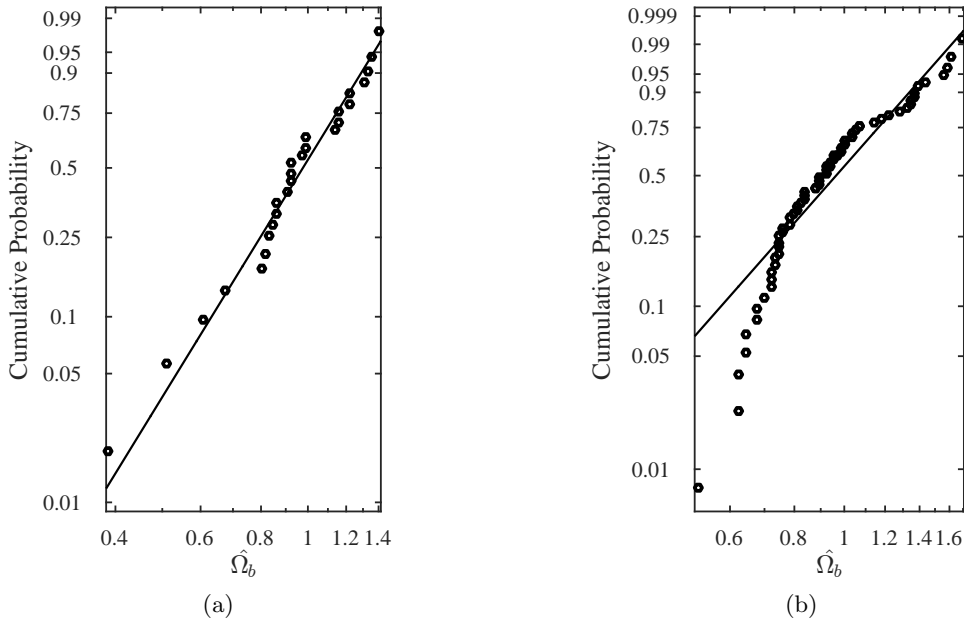Figs. 19a, 19b, 19c and 19d present the crest front wave steepness (ε), the crest rear wave

Figure 17: CDF fits in Weibull scale for the normalized breaker height index $\hat{\Omega}_b$ for (a) case A1 ($H_{so} = 0.30$ m, $T_p = 2.9$ s, s=0.023) b) case B1 ($H_{so} = 0.55$ m, $T_p = 2.0$ s, s=0.088). Open circles for numerical data; solid black line for Weibull fit (for details of the CDF fits, see Table 3)
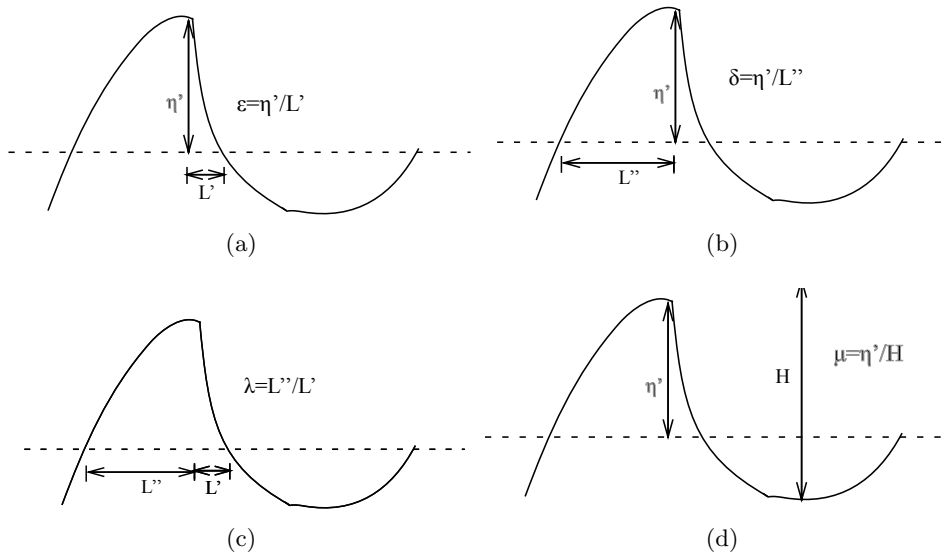

Figure 18: Definitions of wave profile geometry (Kjeldsen and Myrhaug, 1978) a) crest front wave steepness ε; b) crest rear wave steepness δ; c) vertical asymmetry factor λ; d) horizontal asymmetry factor μ

steepness (δ), the horizontal asymmetry factor (μ) and the vertical asymmetry factor (λ), respectively, versus the surf similarity parameter at breaking (ξ_b) for cases A1 and B1. The crest front steepness (ε) shows a slight decreasing trend as ξ_b increases for both cases A1 and B1 (Figs. 19a). The values of ε for case B1 are slightly larger than for case A1, which is dominated by plunging breakers. The crest rear steepness (δ) shows a slight increasing trend as ξ_b increases for both, case A1 (dominated by spilling breakers) and case B1 (plunging breakers) (Fig. 19b). The wave crest becomes more steep and skewed when the irregular wave train propagates for spilling breakers compared to plunging breakers.
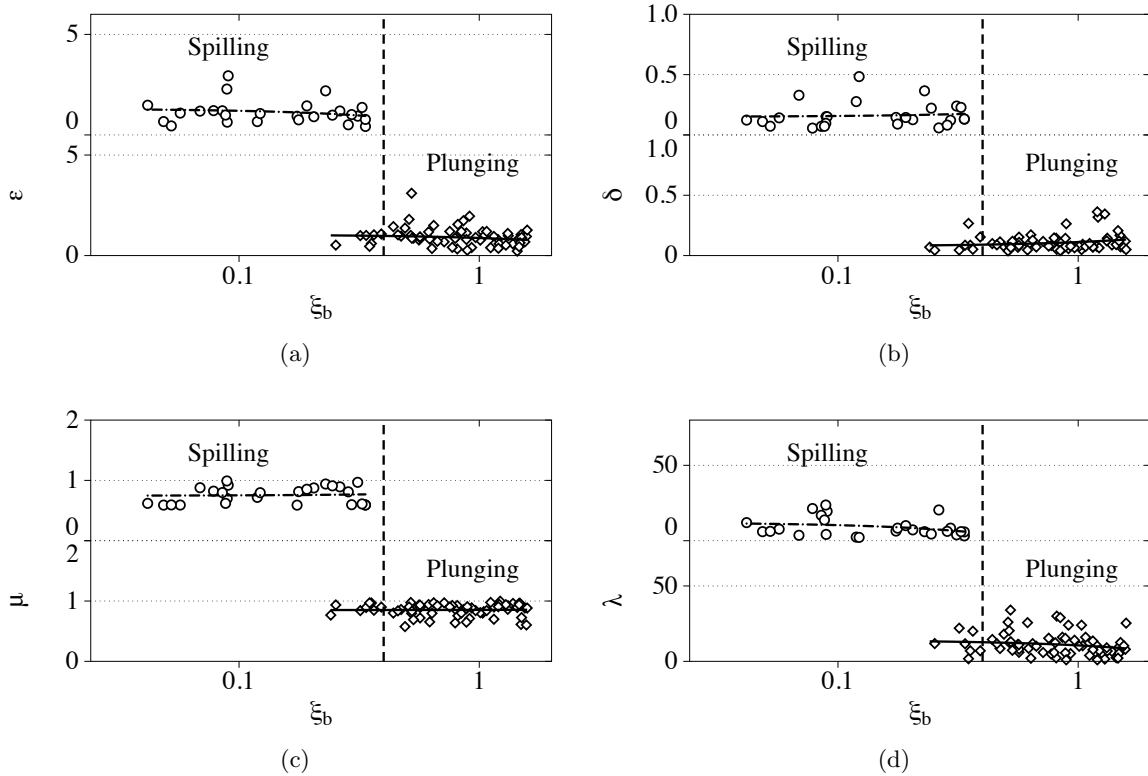

Figure 19: Wave profile geometric properties versus the surf similarity parameter at breaking ξ_b (logarithmic x-axis) for case A1 ($H_{so} = 0.30$ m, $T_p = 2.9$ s, s=0.023) and case B1 ($H_{so} = 0.55$ m, $T_p = 2.0$ s, s=0.088) (a) ε; (b) δ; (c) μ; (d) λ. Upper y-axis shows spilling breakers (case A1) and lower y-axis shows plunging breakers (case B1). Open circles represent case A1; dashed black line is linear fit for case A1; rhombus for case B1; solid black line is linear fit for case B1

It is noticed from Figs. 19c and 19d that μ remains almost invariant, while λ decrease slightly as ξ_b increases for both cases A1 and B1. For the spilling breaker, the front and rear faces of the wave crest become steeper and the forward wave trough flattens at wave breaking. For the plunging breaker, the front face of the wave crest becomes very steep without much change in the rear face of the wave crest and undergoes less deformation.

24

3.8   Correlation of individual breaking and significant breaking wave forces

An irregular wave train is composed of regular wave components of different heights and periods. Each breaking event can have a different breaker location, different breaker type and different breaker shape. The geometric criteria based on the wave slope limit is used to determine breaking waves (Kjeldsen and Myrhaug, 1978; Bonmarin, 1989). The percentage of breaking waves P_b is defined as:

$$P_b = \frac{N_b}{N_i} \times 100 \tag{21}$$

where N_b is the number of breaking waves and N_i is the number of incident waves.

Figs. 20a and 20b present the percentage of breaking waves P_b and the significant value of the irregular breaking wave force F_s versus the spectral wave steepness s as a bar graph. For cases A1-A4 (same T_p and varying H_{so}), both the magnitude of the significant force and the percentage of breaking waves in the irregular wave train increase as the spectral wave steepness increases. P_b and F_s increase by almost 94 % and 140 %, respectively, as s increases from 0.023 (case A1) to 0.046 (case A4) (Fig. 20a). In case A4, a larger number of breaking waves impact the cylinder with large mass of water and exert larger F_s. When the wave steepness is changed by keeping H_{so} constant and by changing T_p (cases A3 and B1-B3; see Table 2), it is observed that the number of breaking waves increases as the wave steepness increases, but the value of the significant wave force F_s first increases and then decreases as s increases. For case B1 ($s = 0.088$), 33.4 % of the waves break, but they break further offshore far away from the cylinder due to a large s. They lose most of their energy when they reach the cylinder and the value of F_s is lower, even though the number of breaking waves in the irregular wave train is larger. Fig. 21 shows the CDF of the normalized $\hat{F}_s$ ($\hat{F}_s = F_s/F_s^{rms}$)
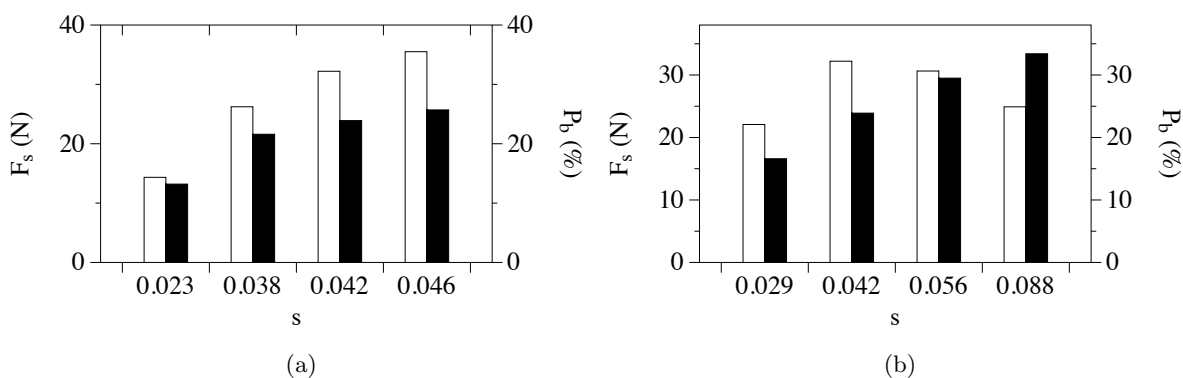

Figure 20: Bar representation of the percentage of breaking waves P_b and significant breaking wave force F_s versus spectral wave steepness s for (a) cases A1 (s=0.023), A2 (s=0.038), A3 (s=0.042) and A4 (s=0.046) (b) cases A3 (s=0.042), B1 (s=0.088), B2 (s=0.056) and B3 (s=0.029). White bar represent F_s and corresponds to the values on left y-axis; black bar represent P_b and corresponds to the values on right y-axis

for all cases (A and B). It appears that the Weibull distribution represents the data quite well for $\hat{F}_s$ >0.8, see Table 3 for the details of the Weibull parameters.
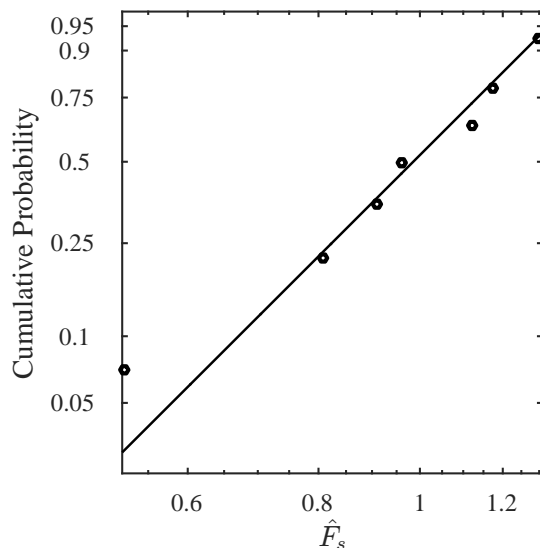
Figure 21: CDF in Weibull scale for the normalized breaking significant irregular wave force $\hat{F}_s$ for all cases A1 (s=0.023), A2 (s=0.038), A3 (s=0.042), A4 (s=0.046), B1 (s=0.088), B2 (s=0.056) and B3 (s=0.029). Circles represent numerical data; black solid line for Weibull fit

3.9 Changes in the horizontal wave-induced water particle velocities at the free surface

During the shoaling and breaking processes, the wave-induced water particle velocities vary due to the change in water depth and wave heights. In order to understand this, the variations in the horizontal wave-induced water particle velocities at the free surface and the velocity spectra are investigated for the horizontal velocity components at the velocity probes located before, at and after the cylinder. The velocity spectrum $\hat{S}_u$ is normalised according to the following equation:

$$\hat{S}_u = \frac{S_u}{T_p(\sqrt{gd})^2} \tag{22}$$

Fig. 22 presents the variation of the normalized horizontal velocity spectrum $\hat{S}_u$ for irregular breaking waves versus frequency f for (a) case A1 ($s = 0.023$) (b) case B1 ($s = 0.088$). For the case with $s = 0.023$, the probe located before the cylinder (P1) estimates the wave velocities during the wave shoaling process (Fig. 22a). The number of breaking wave components in the irregular wave train for this case is low. The wave particle velocity increases due to wave shoaling until the waves reach the cylinder (P2) which is noticed by a slightly higher spectral peak value. After the waves interact with the cylinder, they experience reflections from the cylinder. Some shorter waves are generated due to the wave decomposition process after breaking and the secondary spectral peaks in the velocity spectra become significant (Fig. 22a) (Kamath et al., 2017).

The role of shorter components and their coherence with the spectral peak components is further studied by computing bicoherence for this case (case A1, $s = 0.023$) as shown in Fig. 23. A strong coupling is observed at the peak frequencies (f_p, f_p) and between f_p

and frequencies around $2f_p$. This means that a major portion of the shorter components generated with frequencies around $2f_p$ contribute to the spectral peak and are bound waves (Doering and Bowen, 1995). Furthermore, other components contribute to secondary peaks at higher frequencies in the spectrum as observed by the weak coupling between them and behave as free waves. In the higher spectral wave steepness case B1 ($s = 0.088$), the wave breaking occurs farther offshore at larger water depths. The waves lose a significant amount of their incident wave energy during the wave breaking process before the cylinder (P1) and non-linearity in the wave train is further enhanced. A similar trend was also observed for the wave spectra signifying the contribution of shorter wave components towards the higher frequencies. However, the frequencies at $2f_p$ in the wave spectra behave as bound waves and contribute to the spectral peak. When the waves reach the cylinder on the flat bed (P2), they further lose their energy which reduces the particle velocities as observed by the lower velocity spectrum peak. However, the contribution of the particle velocities for the higher frequencies (>0.4 Hz) is still about the same as at P1. After the waves have interacted with the cylinder, the velocity probe located after the cylinder (P3) shows the further reduced values of the spectral peaks (Fig. 22b). The wave-induced water particle velocities are likewise reduced as noticed by the reductions in both the primary and secondary spectral velocity peaks. This corresponds to the decrease of the wave spectrum computed at this location due to the loss of energy during the wave breaking process.
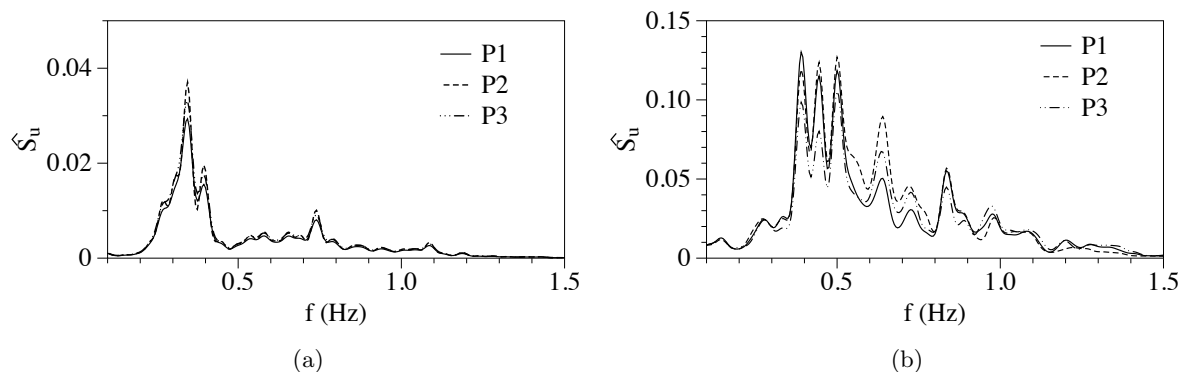

(a)

(b)

Figure 22: Normalized numerical horizontal velocity spectrum $\hat{S}_u$ versus frequency f at different probe locations at free surface for (a) case A1 ($H_{so} = 0.30$ m, $T_p = 2.9$ s, s=0.023) b) case B1 ($H_{so} = 0.55$ m, $T_p = 2.0$ s, s=0.088). X and Y coordinates (in metres) of P1, P2 and P3 are (11.59, 0.20), (13.41, 0.15), (15.59, 0.20), respectively

3.10 Changes in the local pressure at the free surface

The total pressure exerted by the waves during the wave-structure interaction plays a major role in estimating the wave forces. The variations in the wave pressure at the free surface for breaking irregular waves are investigated in the frequency-domain by using the pressure spectrum. The pressure spectrum $\hat{S}_P$ is normalised according to the following equation:

$$\hat{S}_P = \frac{S_P}{T_p(\rho g d)^2} \tag{23}$$
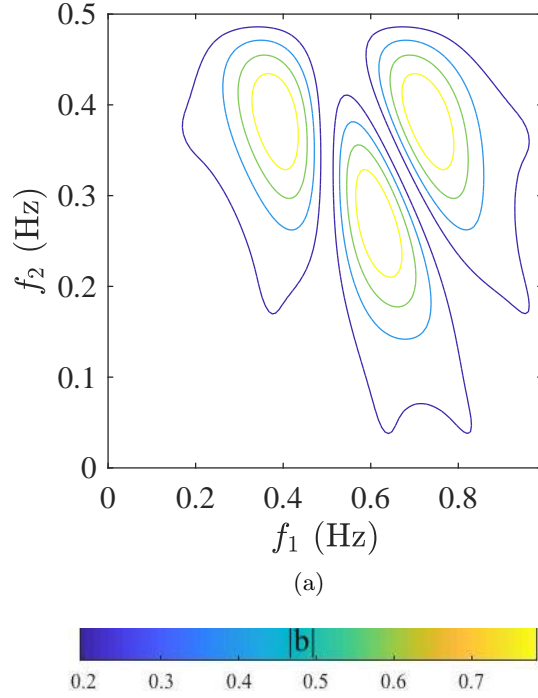
Aggarwal, A. et al., 2019

(a)

Figure 23: Bicoherence estimate for numerical horizontal velocity for case A1 ($H_{so} = 0.30$ m, $T_p = 2.9$ s, $f_p = 0.35$ Hz, s=0.023) at P2 (13.41, 0.15)

where S_P is the pressure spectrum and $\hat{S}_P$ is the normalised pressure spectrum.

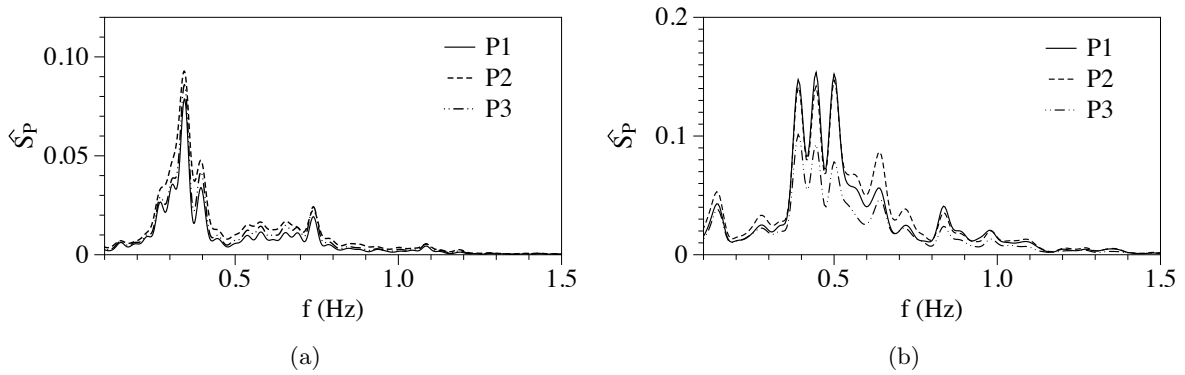(a)   (b)

Figure 24: Normalized numerical pressure spectrum $\hat{S}_P$ versus frequency f at different probe locations at free surface for (a) case A1 ($H_{so} = 0.30$ m, $T_p = 2.9$ s, s=0.023) b) case B1 (H_{so} = 0.55 m, $T_p = 2.0$ s, s=0.088). X and Y coordinates (in metres) of P1, P2 and P3 are (11.59, 0.20), (13.41, 0.15), (15.59, 0.20), respectively

Fig. 24 shows the variation of $\hat{S}_P$ for irregular breaking waves versus the frequency f for (a) case A1 ($s = 0.023$) (b) case B1 ($s = 0.088$). The instantaneous pressure due to waves is associated with the free surface particle velocities. The pressure spectra exhibit behaviours

similar to the horizontal particle velocity spectra for both cases. For the case with the low spectral wave steepness $s = 0.023$, both the primary and secondary spectral peaks before the cylinder (P1) are of lower magnitude compared to $\hat{S}_P$ computed at the cylinder (P2). Most of the individual wave components for the irregular wave train in this case continue shoaling after P1 and attain their maximum wave heights in the vicinity of the cylinder (P2) (Fig. 24a). The increase in the wave heights is associated with the increase in u and consequently, the free surface pressure. This is also noticed in Figs. 4 and 5, where u becomes significantly larger during the breaking process. The spectral peaks of the free surface pressure are slightly reduced after the wave train has interacted with the cylinder (P3), since some of the waves break in the vicinity of the cylinder (P2) and lose their energy (Fig. 24a). In the higher spectral wave steepness case B1 ($s = 0.088$), the number of individual wave components with larger wave steepnesses is higher, leading to offshore wave breaking farther away from the cylinder for most of the waves (Fig. 24b). On further wave propagation over the slope, the additional wave breaking leads to the reduced peaks of the pressure spectrum measured in the vicinity of the cylinder (P2) and after the cylinder (P3), unlike case A1.

Fig. 25 shows the CDF of the normalized $\hat{P} = P/P_{rms}$ (normalized peak values of the free surface pressure in the time-series data) measured at the probe located at the cylinder (P2). It is noticed from Fig. 25a that for case A1 ($H_{so} = 0.30$ m, $T_p = 2.9$ s, s=0.023), where wave breaking is dominated by spilling breakers, the Weibull distribution is appropriate for $\hat{P} > 0.01$. For case B1 ($H_{so} = 0.55$ m, $T_p = 2.0$ s, s=0.088), the Weibull distribution is a reasonable fit for $\hat{P} > 0.0001$, see Table 3 for the details of the Weibull parameters (Fig. 25b).
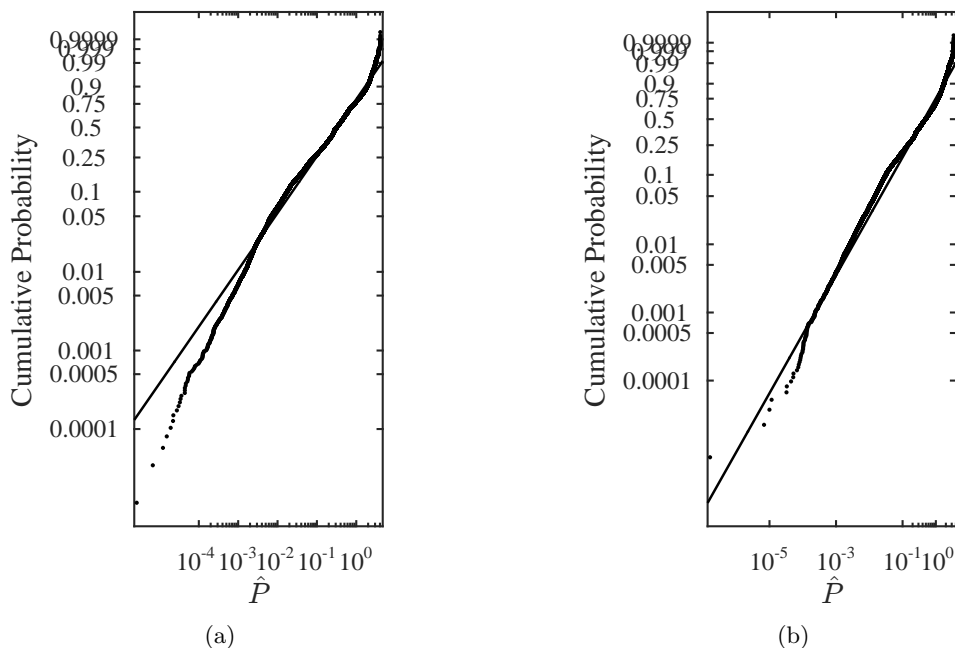

(a)   (b)

Figure 25: CDFs in Weibull scale for the normalized peak values of the total free surface pressure $\hat{P}$ measured at the probe located at the cylinder (P2) (a) case A1 ($H_{so} = 0.30$ m, $T_p = 2.9$ s, s=0.023) (b) case B1 ($H_{so} = 0.55$ m, $T_p = 2.0$ s, s=0.088). Circles represent numerical data; black solid line for Weibull fit

		Weibull parameters	
		a	b
Normalized breaker depth index $\hat{\gamma}_b$	case A1 (s=0.023)	0.96	1.62
	case B1 (s=0.088)	0.95	1.57
Normalized breaker height index $\hat{\Omega}_b$	case A1 (s=0.023)	1.06	4.33
	case B1 (s=0.088)	1.06	3.66
Normalized total peak free surface pressure $\hat{P}$	case A1 (s=0.023)	0.52	0.72
	case B1 (s=0.088)	0.50	0.65
Normalized breaking significant irregular wave force $\hat{F}_s$	all cases A1 -B3	1.06	4.90

Table 3: Table listing the details for different statistical parameters for the Weibull distribution
.

4 Conclusions

A two-phase flow CFD model is used for the numerical investigation of irregular breaking wave forces on a cylinder mounted on a slope. The numerical model is validated for breaking irregular waves and the resulting breaking wave forces on a vertical cylinder. The numerical results for the irregular wave free surface elevation at different wave gauge locations and breaking irregular wave forces are compared with the experiments by Chakrabarti et al. (1997) and a good agreement is obtained with the experimental data for the free surface elevation and the wave force. An extensive numerical analysis is performed to study breaking irregular wave forces by carrying out the investigations for multiple incident irregular wave trains propagating over the slope. Further, alternative simulations with a cylinder moved as a function of a breaking point can be run for the future investigations. First, the wave height transformations and the energy level evolution during the wave breaking process are investigated. The incident wave parameters play a major role in affecting the spectral wave parameters and breaking wave forces. The transformations in the skewness and spectral bandwidth during the wave breaking process are also highlighted. The breaking wave forces are further correlated with the skewness and spectral bandwidth. The dominant wave breaker type and the influence of wave deformation on wave breaking process is also investigated for lowest and highest spectral wave steepness cases. The wave breaking is associated with the changes in the local wave kinematics. The changes in the horizontal wave-induced water particle velocity at the free surface and the free surface wave pressure during the wave breaking process in the vicinity of the cylinder are analysed in the frequency-domain. The following conclusions can be drawn from the study:

- For a given slope, the value of the significant wave force increases as spectral wave steepness increases (for constant offshore H_{so} and different T_p) for irregular waves up to a certain spectral steepness ($s = 0.046$). As the wave steepness increases further, the

wave breaking shifts offshore and the waves break at larger water depths. As a result, they lose a considerable amount of their incident energy before they impact the cylinder and exert wave forces of lower magnitude.

- The spilling breakers dominate the wave breaker type for the cases with lower spectral steepness ($s = 0.023$), they undergo more deformation. While, wave breaking is dominated by plunging breakers for the cases with highest spectral steepness ($s = 0.088$), such waves in the irregular wave train break experience more reflections from the slope due to larger surf similarity parameter.

- Many shorter wave components are generated after wave breaking. The components with frequencies around $2f_p$ behave as bound waves and contribute to the spectral peak as shown by the bicoherence amplitude spectrum. Furthermore, shorter waves with other frequencies behave as free waves and contribute to the multiple peaks in the force and velocity spectra.

- In general, the non-linear energy transfer from the spectral peak region ($f/f_p = 0.9$-1.1) to the above peak region ($f/f_p = 1.2$-1.5) and higher-frequency region ($f/f_p = 1.5$-2.5) during the wave transformation process influences the changes in free surface elevation skewness and spectral bandwidth. Further, the value of the significant wave force is large, when the spectral bandwidth is large. A large bandwidth represents the wave transformation processes; increased wave shoaling and wave breaking and thus large breaking wave forces are observed.

- The horizontal wave-induced water particle velocities at the free surface are significant in estimating the total pressure under waves during the wave breaking process. The wave breaking location is important in determining the secondary and tertiary spectral peaks during the spectral evolution of the velocity and pressure spectra.

- Overall, the Weibull distribution represents higher values of the numerical data reasonably well for the breaker depth index, breaker height index, peak free surface pressure and significant value of the breaking irregular wave force.

Acknowledgements

References

Aggarwal, A., Alagan Chella, M., Kamath, A., Bihs, H. and Arntsen. A., Ø. (2016a). Irregular wave forces on a large vertical circular cylinder. *Energy Procedia*, **94**, 504–516.

Aggarwal, A., Alagan Chella, M., Kamath, A., Bihs, H. and Arntsen. A., Ø. (2016b). Numerical simulation of irregular wave forces on a horizontal cylinder. *35th Proceedings of the ASME International Conference on Ocean, Offshore and Arctic Engineering.*

Alagan Chella, M., Bihs, H., Myrhaug, D. and Michael, M. (2016). Hydrodynamic characteristics and geometric properties of plunging and spilling breakers over impermeable slopes. *Ocean Modelling*, **103**, 53–72.

Alagan Chella, M., Bihs, H., Myrhaug, D. and Michael, M. (2017). Breaking solitary waves and breaking wave forces on a vertically mounted slender cylinder over an impermeable sloping seabed. *Journal of Ocean Engineering and Marine Energy*, **3(1)**, 1–19.

Apelt, J.C. and Piorewicz, J. (1987). Laboratory studies of breaking wave forces acting on vertical cylinders in shallow water. *Coastal Engineering*, **11**, 263–282.

Banner, L.M. and Peregrine, H.D. (1993). Wave breaking in deep water. *Annual Review Fluid Mechanics*, **25**, 373–397.

Battjes, J, A. (1974). Surf similarity. *Proceedings of the 14th International Conference Coastal Engineering, American Society of Civil Engineers, New York*, 466–480.

Berthelsen, P.A. and Faltinsen, O.M. (2008). A local directional ghost cell approach for incompressible viscous flow problems with irregular boundaries. *Journal of Computational Physics*, **227**, 4354–4397.

Bihs, H. and Kamath, A. (2017). A combined level set/ghost cell immersed boundary representation for simulations of floating bodies. *International Journal for Numerical Methods in Fluids*, **83(12)**, 905–916.

Bihs, H., Kamath, A., Alagan Chella, M., Aggarwal, A. and Arntsen. A., O. (2016*a*). A new level set numerical wave tank with improved density interpolation for complex wave hydrodynamics. *Computers and Fluids*, **140**, 191–208.

Bihs, H., Kamath, A., Alagan Chella, M. and Arntsen. A., O. (2016*b*). Breaking-wave interaction with tandem cylinders under different impact scenarios. *Journal of Waterway, Port, Coastal, and Ocean Engineering*, **142(5)**, 1–14.

Bonmarin, P. (1989). Geometric properties of deep water breaking waves. *Journal of Fluid Mechanics*, **209**, 405–433.

Bredmose, H. and Jacobsen, N., G. (2010). Breaking wave impacts on offshore wind turbine foundations: focused wave groups and CFD. *Proceedings of the 29th International Conference on Ocean, Offshore and Arctic Engineering, Shanghai, China*.

Chakrabarti, S.K., Kriebel, D. and Berek, E. (1997). Forces on a single pile caisson in breaking waves and current. *Applied Ocean Research*, **19**, 113–140.

Chan, E., S. and Melville, W., K. (1988). Deep-water plunging pressures on a vertical plane wall. *Proceedings of the Royal Society of London, London, England,*, **A417**, 95–131.

Choi, S., Lee, K. and Gudemestad, O. (2015). The effect of dynamic amplification due to a structures vibration on breaking wave impact. *Ocean Engineering*, **96**, 8–20.

Chorin, A.J. (1968). Numerical solution of the Navier-Stokes equations. *Mathematics of Computation*, **22**, 745–762.

Christensen, D.E., Bredmose, H. and Hansen, A., E. (2005). Extreme wave forces and wave run-up on offshore windturbine foundations. *Proceedings of Copenhagen Offshore Wind*, 1–10.

Det Norske Veritas (DNV) (2010). Design of offshore wind turbine structures. *OS-J101*.

Doering, J. and Bowen, A. (1995). Parametrization of orbital velocity asymmetries of shoaling and breaking waves using bispectral analysis. *Coastal Engineering*, **26**(1-2), 15–33.

Elgar, S. and Guza, R. (1985). Observations of bispectra of shoaling surface gravity waves. *Journal of Fluid Mechanics*, **161**, 425–448.

Elgar, S., Guza, T.R., Raubenheimer, B., Herbers, C.H.T. and Gallagher, L.E. (1997). Spectral evolution of shoaling and breaking waves on a barred beach. *Journal of Geophysical Research*, **102**, 15797–15805.

Falgout, R.D. and Yang, U.M. (2002). HYPRE: A library of high performance preconditioners. **Springer Berlin Heidelberg**, 632–641.

Goda, Y. (2010). Reanalysis of regular and random breaking wave statistics. *Coastal Engineering*, **52**, 71–106.

Goda, Y., Haranaka, S. and Kitahata, M. (1966). Study of impulsive breaking wave forces on piles. *Report of Port and Harbor Research Institute*, **5(6)**, 1–30.

Griebel, M., Dornseifer, T. and Neunhoeffer, T. (1998). *Numerical Simulations in Fluid Dynamics*. SIAM.

Hajime, M. and Kirby, T.J. (1992). Hybrid frequency-domain KdV equation for random wave transformation. *Philosophical Transactions: Mathematical, Physical and Engineering Sciences*, **354(1707)**, 649–676.

Hieu, D., Katsutoshi, T. and Ca, T.V. (2004). Numerical simulation of breaking waves using a two-phase flow model. *Applied Mathematics Modelling,*, **28**, 983–1005.

Jacobsen, N.G., Fuhrman, D. and Fredsøe, J. (2012). A wave generation toolbox for the open-source CFD library: Openfoam®. *International Journal for Numerical Methods in Fluids*, **70**, 1073–1088.

Jiang, J. and Shu, C.W. (1996). Efficient implementation of weighted eno schemes. *Journal of Computational Physics*, **126**, 202–228.

Kamath, A., Alagan Chella, M., Bihs, H. and Arntsen, A., Ø. (2016*a*). Breaking wave interaction with a vertical cylinder and the effect of breaker location. *Ocean Engineering*, **128**, 105–115.

Kamath, A., Alagan Chella, M., Bihs, H. and Arntsen, A., Ø. (2016*b*). Upstream and downstream cylinder influence on the hydrodynamics of a four cylinder group. *Journal of waterway, port, coastal, and ocean engineering.*, **142(4)**, 04016002.

Kamath, A., Alagan Chella, M., Bihs, H. and Arntsen., A., Ø. (2017). Energy transfer due to shoaling and decomposition of breaking and non-breaking waves over a submerged bar. *Engineering Applications of Computational Fluid Mechanics*, **11(1)**, 450–466.

Kjeldsen, S.P. and Myrhaug, D. (1978). Kinematics and dynamics of breaking waves. *Technical Report. River and Harbour Laboratory (NHL) — The Norwegian Institute of Technology.*

Lin, P. and Liu, L. (1998). A numerical study of breaking waves in the surf zone. *Journal of Fluid Mechanics*, **359**, 239–264.

Longuet-Higgins, M.S. (1975). On the joint distribution of the periods and amplitudes of sea waves. *Journal of Geophysical Research*, **80**, 2688–2693.

Mayer, S., Garapon, A. and Sø rensen, S.L. (1998). A fractional step method for unsteady free surface flow with applications to non-linear wave dynamics. *International Journal of Numerical Mathematics and Fluids*, **28**, 293–315.

Mo, W., Jensen, A. and Liu, P. (2013). lunging solitary wave and its interaction with a slender cylinder on a sloping beach. *Ocean Engineering*, **74**, 48–60.

Osher, S. and Sethian, J.A. (1988). Fronts propagating with curvature- dependent speed: Algorithms based on hamilton-jacobi formulations. *Journal of Computational Physics*, **79**, 12–49.

Oumeraci, H., Klammer, P. and Partenscky, W., H. (1993). Classification of breaking wave loads on vertical structures. *Journal of Waterway, Port, Coastal, Ocean Engineering*, **119(4)**, 381–397.

Paulsen, T., B., Bredmose, H., Bingham, B, H. and Schloer, S. (2013). Steep wave loads from irregular waves on an offshore wind turbine foundation: computation and experiment. *32nd Proceedings of the ASME International Conference on Ocean, Offshore & Arctic Engineering.*

Rattanapitikon, W. and Shibayama, T. (1998). Energy dissipation model for irregular breaking waves. *Coastal Engineering Proceedings*, 112–125.

Schaffer, A.H. and Klopman, G. (2000). Review of multidirectional active wave absorption methods. *Journal of the Waterway, Port, Coastal and Ocean Engineering*, **126**, 88–97.

Shu, C.W. and Oscher, S. (1988). Efficient implementation of essentially non-oscillatory shock capturing schemes ii. *Journal of Computational Physics*, **77**, 439–471.

Tanimoto, K., Takahashi, S., Kaneko, T. and Shiota, K. (1986). Impulsive breaking wave forces on an inclined pile exerted bi random waves. *Proceedings of Coastal Engineering.*

Tian, Z., Perlin, M. and Choi, W. (2011). Frequency spectra evolution of two-dimensional focusing wave groups in finite depth water. *Journal of Fluid Mechanics*, **688**, 169–194.

Wilcox, D. (1994). Turbulence modeling for CFD. *DCW Industries Inc. La Canada, California.*

Zhao, Q., Armfield, S. and Tanimoto, K. (2004). Numerical simulation of breaking waves by a multi-scale turbulence model. *Coastal Engineering*, **51**, 53–80.